

Chapter 5

The mechanism of Ni(*i*Pr–pybox) complexes as asymmetric Negishi C–C coupling catalysts

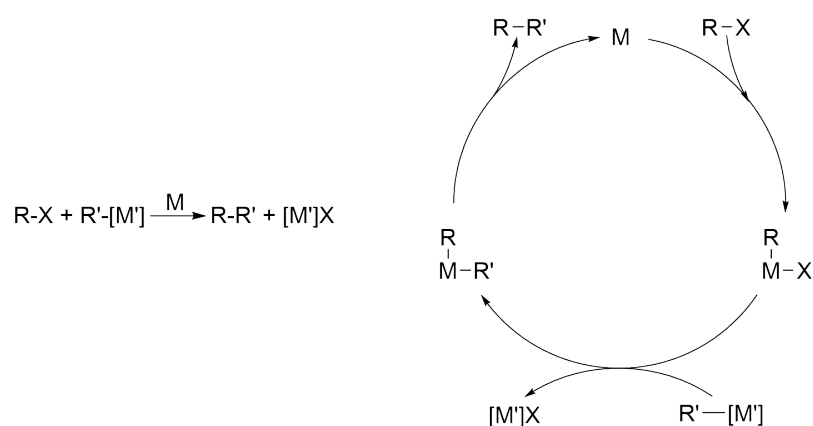
5.1 Abstract

The 2,6-bis(4-isopropyl-2-oxazolin-2-yl)pyridine (*i*Pr–pybox) ligand, when combined with a nickel salt in *N,N*-dimethylacetamide (DMA), generates an *in situ* Ni(*i*Pr–pybox) complex that catalyzes enantioselectively the cross-coupling of secondary *sp*³-C substrates. This system is very notable for its property of stereoconvergence: *both* enantiomers of a racemic substrate may be converted into a single enantiomer of a product. This chapter will computationally explore the mechanism responsible for both the remarkable activity and selectivity of the Ni(*i*Pr–pybox) system; such a mechanism is believed to deviate substantially from the canonical “textbook” mechanism of Negishi coupling. Furthermore, a generalized calculation scheme is presented that allows for the rapid enantioselectivity prediction of many related pybox ligands as well, in order to help predict the next generation of asymmetric Negishi coupling catalysts.

5.2 Introduction

The controlled formation of C–C bonds is one of the central challenges of synthetic organic chemistry. Generally, the cross-coupling of two distinct organic moieties R and R' is done by selecting precursors with opposite polarity, for example, an electrophilic R–X (where X is a leaving group) along with a nucleophilic R'–[M'] (where M' is a less electronegative element, often a main-group metal or metalloid). Late transition metals M are typically added as well in order to catalyze activity and encourage the formation of R–R' as opposed to undesired side products. Ligands may also be added in order to further enhance the activity of the transition metal catalyst by the generation of *in situ* complexes.

Scheme 5.1 shows the overall cross-coupling reaction, as well as a general scheme for the mechanism. This mechanism [1] begins with the oxidative addition of R–X by a low-valent M (hence the necessity of using a late transition metal). The X ligand is then exchanged for an R' in the transmetalation step, and finally reductive elimination regenerates the starting M and releases the coupled product R–R'.



Scheme 5.1. Left: the overall C–C bond-forming cross-coupling reaction. Right: the general mechanism for the cross-coupling reaction.

Table 5.1 shows a few examples of cross-coupling reactions. As already mentioned, the electrophile is typically R–X where X is a leaving group such as a halide or sulfonate. Substrates in which the R group is an aryl or alkenyl, or a resonance-stabilized sp^3 radical such as an allyl or propargyl group, tend to be more active. The metal catalyst M is typically Cu, Ni, or Pd, with Pd being the most versatile element but also the rarest and most expensive. The nucleophile is R'–[M'] where M' may well be any element that forms a weaker bond to R' than M, and/or a stronger bond to X.

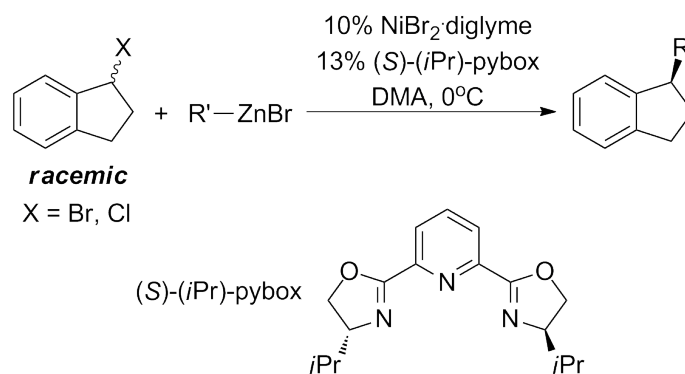
Coupling	Electrophile	Nucleophile	Catalyst	Reference
Kumada	R-X	R'-MgBr	Pd, Ni	[2]
Heck	R-X	alkene	Pd	[3]
Sonogashira	R-X	R'-C≡CH	Pd, Cu	[4]
Negishi	R-X	R'-ZnX	Pd, Ni	[5]
Stille	R-X	R'-SnR' ₃	Pd	[6]
Suzuki	R-X	R'-B(OR'') ₂	Pd	[7]
Hiyama	R-X	R'-SiR' ₃	Pd	[8]

Table 5.1. Examples of various C-C cross-coupling reactions. This list is not exhaustive.

5.2.1 The Ni(*i*Pr-pybox) system

Another central challenge of synthetic organic chemistry is the enantioselective synthesis of chiral compounds. For cross-coupling reactions in which C-C bonds are formed, the carbon atoms being bonded are often chiral centers, necessitating techniques for asymmetric synthesis. For cross-coupling reactions, this may be done by adding a chiral ligand to complex the catalyst metal, thus preferentially coupling only one enantiomer of a racemic starting material. Alternatively, one may also simply begin with an enantiopure substrate and choose a coupling reaction that preserves chirality.

The Ni(*i*Pr-pybox) system, developed by Gregory Fu and coworkers, is a Negishi coupling catalyst that utilizes nickel and the 2,6-bis(4-isopropyl-2-oxazolin-2-yl)pyridine ligand, abbreviated as (*i*Pr-pybox), and couples organic halides to organozinc complexes [9]. The (*i*Pr-pybox) ligand contains two chiral centers and can exist in three diastereomers: the *C*₂ enantiomers ((*R,R*)-*i*Pr-pybox) and ((*S,S*)-*i*Pr-pybox)), and the *C*_s *meso* diastereomer ((*R,S*)-*i*Pr-pybox). If a chiral *C*₂ ligand is used, asymmetric catalysis results. The complex and a summary of its catalytic scope is shown in Scheme 5.2 and Table 5.2 [9, 10].



Scheme 5.2. The general reaction of the Ni(*i*Pr-pybox) Negishi coupling catalyst with benzylic secondary alkyl halides. α -Bromo amides and propargylic halides are also viable substrates that have been studied.

This Ni(*i*Pr-pybox) system is advantageous for several reasons [10]:

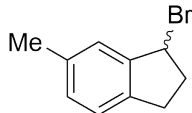
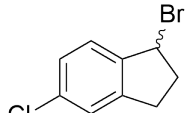
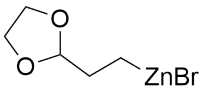
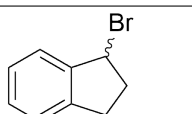
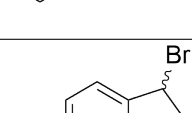
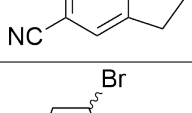
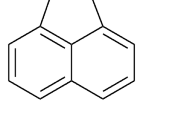
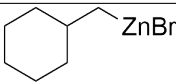
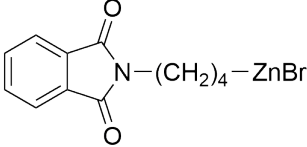
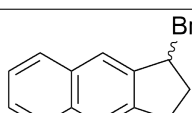
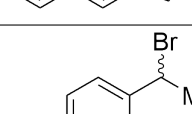
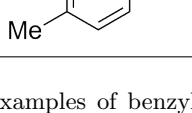
Entry	R-X	R'-ZnBr	Yield (%)	ee (%)
1		C ₆ H ₁₃ -ZnBr	89	96
2			82	91
3		N≡C-(CH ₂) ₃ -ZnBr	64	91
4		Cl-(CH ₂) ₆ -ZnBr	69	94
5		<i>n</i> Bu-ZnBr	47	91
6			72	98
7			39	96
8		Ph-(CH ₂) ₃ -ZnBr	41	99
9		BnO-(CH ₂) ₃ -ZnBr	76	98
10			63	75

Table 5.2. Some examples of benzylic secondary alkyl halide substrates coupled by the Ni(*i*Pr-pybox) catalyst. All reactions were performed under conditions as in Scheme 5.2, except for entries 7 and 8 which were performed at room temperature. The data in this table was taken from Arp and Fu [10].

1. It is a Negishi coupling catalyst, utilizing organozinc reagents as the nucleophile. Organozinc compounds are relatively tractable and accessible;
2. The ligand is known and is not difficult to synthesize from commercially-available starting materials;
3. The system is not particularly oxygen or water sensitive, and the reaction may be run under air;
4. Coupling reactions with alkyl substrates are typically more difficult than with their aryl counterparts, and unwanted side reactions such as β -hydride elimination may be present. Secondary alkyls are particularly problematic due to their added steric bulk. The pybox system has been demonstrated to work with various secondary alkyl electrophiles such as benzylic halides, α -bromo amides, and propargylic halides [11].

However, one of the Ni(*i*Pr-pybox) system's most interesting properties may be its stereoconvergence. A racemic starting material may be used to generate a nearly enantiopure product with high yield (See Scheme 5.2). This implies that the mechanism requires both the destruction of the starting material's stereochemistry as well as the formation of the product's stereochemistry, and indicates that the mechanism may be more complex than the existing "textbook" mechanism as shown in Scheme 5.1.

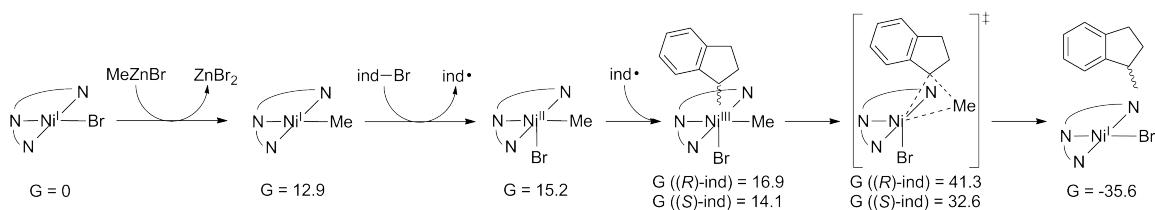
5.2.2 Existing computational work

The mechanism for the Ni(*i*Pr-pybox) system's remarkable reactivity was computationally investigated by Lin et al., who modeled the coupling of 1-bromoindane (the electrophile in Table 5.2, entry 3) with methylzinc bromide as catalyzed by Ni^I((*S,S*)-*i*Pr-pybox)Br to form (*R*)- and (*S*)-1-methylindane [12]. Their results, which are summarized in 5.1, claim that Ni^I((*S,S*)-*i*Pr-pybox)Br is first methylated by methylzinc bromide to form Ni^I((*S,S*)-*i*Pr-pybox)Me. Oxidation by 1-bromoindane results in Ni^{II}((*S,S*)-*i*Pr-pybox)(Me)Br and the indanyl radical, which then recombine to form Ni^{III}((*S,S*)-*i*Pr-pybox)(Me)(Br)(ind) (ind = 1-indanyl), which undergoes reductive elimination to form the 1-methylindane product and to regenerate the Ni^I((*S,S*)-*i*Pr-pybox)Br starting catalyst.

The mechanism put forth by Lin et al. supports the hypothesis of Fu et al. that a Ni^I-Ni^{III} cycle is involved, as opposed to the Ni⁰-Ni^{II} cycle of a classical coupling reaction. In addition, their conclusions show a decisive preference for the formation of the (*S*)-1-methylindane enantiomer, in line with experimental evidence. However, their methodology and analysis have several issues:

1. The density functional theory used, B3LYP, neglects van der Waals interactions, which typically increase in importance for large molecules;

Figure 5.1. The computationally studied mechanism by Lin et al. of Ni(*S,S*)-*i*Pr-pybox catalysis of methyl-indane coupling. The steps are: methylation and oxidation of Ni^I((*S,S*)-*i*Pr-pybox)Br to Ni^{II}((*S,S*)-*i*Pr-pybox)(Me)Br, recombination with indanyl radical to form Ni^{III}((*S,S*)-*i*Pr-pybox)(Me)(Br)(ind), and reductive elimination to form 1-methylindane product. All energies in kcal/mol. Note that for the first two steps (i.e. methylation and oxidation to Ni^{II}), the energy differences are only estimates, as the actual calculations were only performed on the parent Ni(pybox) complexes.



2. The basis set used, 6-31G* (a Pople-type double- ζ Gaussian basis set with polarization functions on non-hydrogen atoms) is rather small and limited, and may lead to inaccurate energies [13];
3. Whereas the authors claim to investigate the enantioselectivity of the Ni(*i*Pr-pybox) system, in many reactions the simplified pybox ligand (without the isopropyl groups) was used in lieu of (*i*Pr)-pybox to simplify calculations;
4. The authors model the methylzinc bromide nucleophile as a simple two-coordinate complex; however, the true nature of the zincate in solution is likely to be much more complex [14];
5. Although the reaction conditions and all experimental investigations have used DMA as the solvent, the authors modeled the reaction in DMSO instead;
6. Only one radical attack pathway (i.e. that of the indanyl radical approaching axially to the Ni) was considered.

Therefore, it is not surprising that enantioselectivity of the Ni(*i*Pr-pybox) system, which can be measured using the metric $\Delta\Delta G^\ddagger := \Delta G_R^\ddagger - \Delta G_S^\ddagger$, was greatly overestimated at 8.7 kcal/mol, whereas the experimentally determined enantiomeric excesses correspond to a $\Delta\Delta G^\ddagger$ value of 2–3 kcal/mol.

Due to these deficiencies, we have undertaken our own computational study of the Ni(*i*Pr-pybox) system's asymmetric catalysis reaction, using larger basis sets, more accurate DFTs and molecular models, and more potential reaction pathways considered. We have found a substantially different mechanism from that of Lin et al., with an overall reaction barrier of 15.9 kcal/mol for the formation of *S*-methylindane and a $\Delta\Delta G^\ddagger$ value of 2.7 kcal/mol, in line with the experimentally determined values [15]. In addition, we have found a useful protocol for the rapid determination of the $\Delta\Delta G^\ddagger$ enantioselectivity values of other related Ni(pybox) systems. We present some new results

and predictions using this new method.

5.3 Materials and methods

For our calculations, the specific reaction we investigated was the coupling of racemic 1-bromoindane with methylzinc iodide to form (*S*)-1-methylindane, using $\text{Ni}^{\text{I}}((S,S)\text{-}i\text{Pr-pybox})\text{Br}$ as a catalyst or precatalyst. The solvent was taken to be DMA and the temperature 258.15 K.

All quantum mechanical calculations were carried out using the Jaguar software version 7.9 developed by Schrödinger Inc. [16]. Geometry optimizations were carried out on initial guess structures, and vibrational frequencies were gathered to confirm the optimized geometries as intermediates or transition states and to construct a free energy profile. Solvation energies were calculated using the PBF Poisson-Boltzmann implicit continuum solvation model [17] in Jaguar, with a dielectric constant of 37.78 [18] and a probe radius of 2.642 Å [19] for DMA.

Geometry optimization and vibrational data were calculated using the B3LYP-D3 density functional [20] with a smaller basis set, whereas single point gas-phase and solvated energies were calculated using the same functional and a larger basis set. The “-D3” suffix refers to the post-SCF correction developed by Grimme et al. that accounts for van der Waals forces [21]. Here the smaller basis set consists of a modified double- ζ Los Alamos basis set and pseudopotential (LACVP**) [22] for transition metals, and the 6-31G** basis set [13] for the other atoms; whereas the larger basis set consists of the triple- ζ Los Alamos basis set and pseudopotential (LACV3P**++) for transition metals, the same LAV3P basis set and pseudopotential for heavy main-group elements, and the 6-311G**++ basis set [23] for the other atoms. Proposed intermediates and transition states were found to have zero and one negative frequencies, confirming their status as local energy minima and saddle points, respectively.

The free energy for each molecular species in solution was calculated using the formula

$$G = E_{\text{gas}} + \Delta G_{\text{solv}} + \text{ZPE} + H_{\text{vib}} + 6kT - T[S_{\text{vib}} + \gamma(S_{\text{trans}} + S_{\text{rot}} - \alpha) + \beta]$$

where the last term (with $\alpha = 14.3$ e.u., $\beta = 7.98$ e.u., and $\gamma = 0.54$) is an empirical approximation for the change in the translational and rotational entropy of the molecule between the gas phase and the solution phase (due to the finite librational frequencies), derived from Wertz [24].

For the monatomic anions Br^- and I^- , the Wertz approximation was not necessary. Hence we used the equation

$$G = E_{\text{gas}} + \Delta G_{\text{solv}} + \frac{5}{2}kT - TS + 1.9$$

to construct the free energy.

For DMA, the Gibbs free energy was calculated using the formula

$$G_{\text{liquid}} = E_{\text{gas}} + \text{ZPE} + H_{\text{tot}} - TS_{\text{tot}} + \Delta G_{\text{gas} \rightarrow \text{liquid}}$$

where $\Delta G_{\text{gas} \rightarrow \text{liquid}} = G_{\text{liquid}} - G_{\text{gas}}(1 \text{ atm})$ is the free energy of condensation to liquid from 1 atm gas. We can solve for this by noting that

$$\Delta G_{\text{gas} \rightarrow \text{liquid}} = \Delta G_{\text{expansion}} + G_{\text{gas} \rightarrow \text{solvation}},$$

where $\Delta G_{\text{expansion}} = G_{\text{gas}}(P) - G_{\text{gas}}(1 \text{ atm})$ is the expansion of the gas from 1 atm to the vapor pressure P , and $G_{\text{gas} \rightarrow \text{solvation}}$ is the condensation of gas at vapor pressure P to liquid. Since a liquid is by definition at equilibrium with its vapor pressure $G_{\text{gas} \rightarrow \text{solvation}} = 0$, and we thus have

$$\Delta G_{\text{gas} \rightarrow \text{liquid}} = G_{\text{gas}}(P) - G_{\text{gas}}(1 \text{ atm}) = RT \ln \left(\frac{P}{1 \text{ atm}} \right).$$

We can find the vapor pressure P at a given temperature using the Antoine Equation:

$$\log_{10} P = A - \frac{B}{C + T},$$

where the empirical parameters A , B , and C vary with the solvent and temperature. For DMA at 258.15 K, $A = 6.0888$, $B = 2725.96$, $C = 28.209$, so the vapor pressure is 3.71×10^{-4} atm [25].

5.4 Results

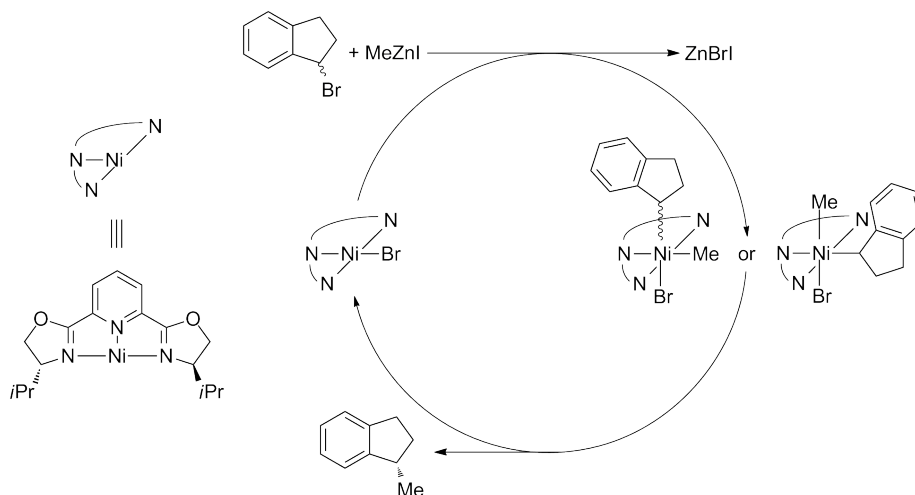
In this section, we present the results of our calculations and the likely mechanism of C–C coupling that the Ni(*i*Pr–pybox) system undergoes. We begin by first outlining the general overarching mechanism, and then examine in depth the details of each step.

5.4.1 The overall general mechanism

In the previous work of Lin et al., the authors claimed early in their report that the Ni⁰-Ni^{II} cycle that a typical Negishi catalyst might undergo had an overall barrier of 57.3 kcal/mol, and consequently was not feasible [12]. Despite our concerns about their methodology (see Section 5.2.2), we do not believe that addressing these concerns would have any potential to lower the barrier enough to make the Ni⁰-Ni^{II} cycle accessible. Hence, we agree with their conclusion that the Ni(*i*Pr–pybox) system most likely goes through a Ni^I-Ni^{III} cycle. We therefore restrict our mechanistic investigations to the Ni^I-Ni^{III} cycle.

Scheme 5.3 shows the Ni^I-Ni^{III} cycle in its most general form. The catalyst alternates between a

Ni^{I} and a Ni^{III} state (for example, $\text{Ni}^{\text{I}}((S,S)\text{-}i\text{Pr-pybox})\text{Br}$ and $\text{Ni}^{\text{III}}((S,S)\text{-}i\text{Pr-pybox})(\text{Me})(\text{Br})(\text{ind})$, respectively). Conversion of $\text{Ni}^{\text{I}}((S,S)\text{-}i\text{Pr-pybox})\text{Br}$ to $\text{Ni}^{\text{III}}((S,S)\text{-}i\text{Pr-pybox})(\text{Me})(\text{Br})(\text{ind})$ should proceed *via* methylation and addition of indanyl and bromine radicals, in any order. Conversion of $\text{Ni}^{\text{III}}((S,S)\text{-}i\text{Pr-pybox})(\text{Me})(\text{Br})(\text{ind})$ back to $\text{Ni}^{\text{I}}((S,S)\text{-}i\text{Pr-pybox})\text{Br}$ should proceed *via* reductive elimination of 1-methylindane. The rest of this section will examine the detailed pathways of this generalized scheme.



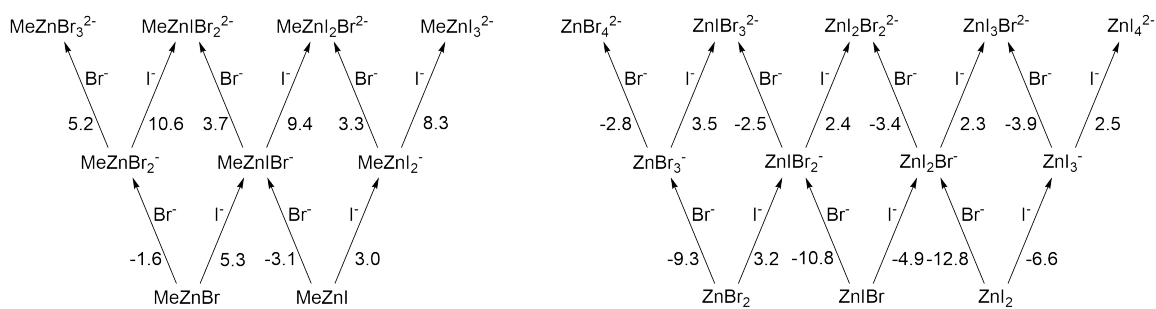
Scheme 5.3. The generalized mechanism of the $\text{Ni}(i\text{Pr-pybox})$ Negishi coupling catalyst as it proceeds through a $\text{Ni}^{\text{I}}\text{-Ni}^{\text{III}}$ cycle. The overall equation is $\text{ind-Br} + \text{MeZnI} \longrightarrow \text{ind-Me} + \text{ZnBrI}$.

5.4.2 Nature of the organozinc reagent

In order to address how alkyl transfer of the methylzinc iodide to the $\text{Ni}(i\text{Pr-pybox})$ complex occurs, it is necessary to first identify the exact nature of the methyl transferring species. Lin et al. depict the complexation of $\text{Ni}(\text{pybox})$ with a simple two-coordinate linear MeZnBr species in their calculations; however, it is unclear if such an electron-deficient species is at all present in a strongly polar solvent such as DMA. Indeed, the active methylation species has often been assumed to be a three coordinate MeZnX_2^- [26]. Recent titration work by Organ et al. suggests, however, that the true methylating species is in fact four-coordinate dianionic MeZnX_3^{2-} with a Pd catalyst and a THF or THF/DMI 2:1 solvent (THF = tetrahydrofuran; DMI = *N,N'*-dimethyl-2-imidazolidinone) [14].

For our mechanistic investigation, we decided to undertake a comprehensive computational investigation of the methylzinc and inorganic zinc species that may be present in the DMA solution under reaction conditions. Scheme 5.4 shows our calculated free energies of complexation of MeZnX and ZnX_2 with one and two equivalents of X^- , where X may be either bromine or iodine. We found that, contrary to the results of Organ et al., three-coordinate MeZnX_2^- species are preferred; this discrepancy may be due to our choice of DMA as solvent, which has a much larger dielectric constant

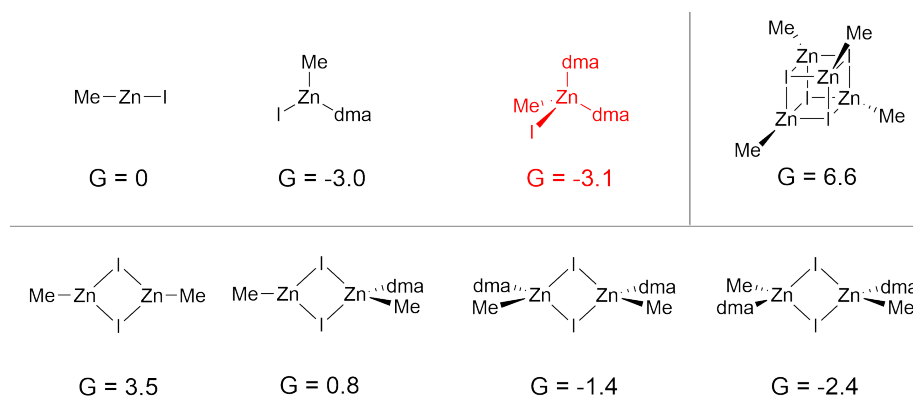
of 37.78 compared to the THF as used by Organ et al. ($\epsilon = 7.2$).



Scheme 5.4. Complexation of the various MeZnX (left) and ZnX₂ (right) species with X⁻, where X ∈ {Br, I}. Numbers next to each arrow are the free energy change for the specific reaction. All numbers in kcal/mol.

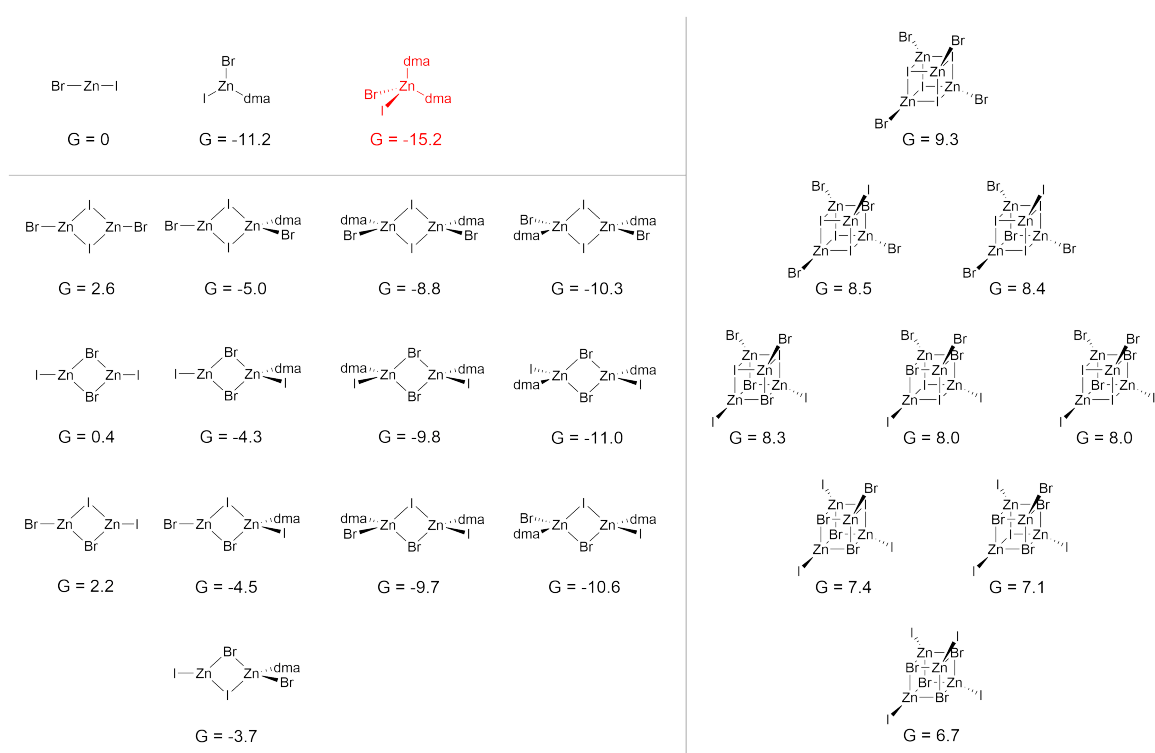
We also considered the possibility that the zinc species might form adducts with DMA, or cluster into polynuclear complexes. Given the strong polarity of the DMA solvent, we expected the former possibility to be more likely, but both pathways were explored. Figure 5.2 shows the various adducts and cluster complexes of MeZnX, whereas Figure 5.3 shows the various adducts and cluster complexes of ZnX₂.

Figure 5.2. The various (MeZnI)_m(dma)_n species, where *m* may equal 0 (top row, left), 1 (bottom row), or 2 (top row, right); and *n* may equal 0, 1, or 2 as well. All numbers are free energies in kcal/mol and relative to MeZnI. The lowest energy species, MeZnI(dma)₂, is highlighted in red.



Our results show that the most stable methylzinc species are MeZnBrI⁻ and MeZnI(dma)₂, at -3.1 kcal/mol relative to the base MeZnI; and that the most stable inorganic zinc species is ZnBrI(dma)₂, at -15.2 kcal/mol relative to the base ZnBrI. For consistency, we have set MeZnI(dma)₂ to be our active methylating agent and ZnBrI(dma)₂ to be our ultimate product. Therefore, the overall reaction that we are investigating can now be written as ind-Br + MeZnI(dma)₂ → ind-Me + ZnBrI(dma)₂.

Figure 5.3. Left: The various $(\text{ZnBrI})_m(\text{dma})_n$ species, where m may equal 0 (first row) or 1 (second to fifth rows); and n may equal 0 (first column), 1 (second column), or 2 (third and fourth columns). Right: The various $(\text{ZnBrI})_4$ tetrameric clusters. All numbers are free energies in kcal/mol and relative to ZnBrI . The lowest energy species, $\text{ZnBrI}(\text{dma})_2$, is highlighted in red.



5.4.3 Mechanism for Ni^I oxidation and methylation

We now address the mechanistic steps that must be taken for the top half of the cycle in Scheme 5.3, i.e. the conversion of Ni^I((*S,S*)-*iPr*-pybox)Br to Ni^{III}((*S,S*)-*iPr*-pybox)(Me)(ind)Br. This conversion is expected to proceed through methylation with MeZnI(dma)₂ and oxidation with ind-Br. Due to the stereoconvergent nature of the catalysis, in which the prior stereochemistry of the starting ind-Br is destroyed, the oxidation is not expected to be a typical one-step oxidative addition reaction. Instead, there is believed to be an initial one-electron oxidation in which Ni^{II} and a benzylic-stabilized indanyl radical are produced, followed by recombination to form the Ni^{III} species. These assertions are supported by experimental evidence (i.e. the formation of coupling products [15]), and the calculations of Lin et al. [12] support their feasibility.

As a result, we have three possibilities for the conversion of Ni^I((*S,S*)-*iPr*-pybox)Br to Ni^{III}((*S,S*)-*iPr*-pybox)(Me)(ind)Br:

The Ni^I pathway: Methylation occurs first, converting Ni^I((*S,S*)-*iPr*-pybox)Br to Ni^I((*S,S*)-*iPr*-pybox)Me, and subsequent oxidation by ind-Br produces Ni^{III}((*S,S*)-*iPr*-pybox)(Me)(ind)Br;

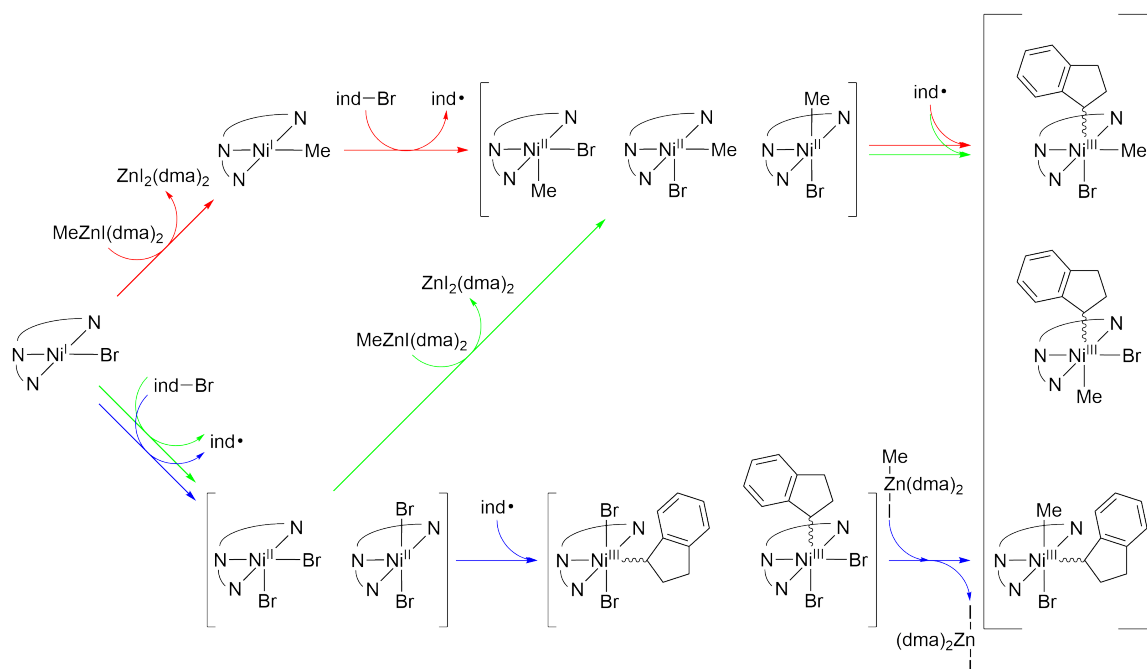
The Ni^{II} pathway: Oxidation by ind-Br to Ni^{II}((*S,S*)-*iPr*-pybox)Br₂ and free indanyl radical occurs first. Methylation to Ni^{II}((*S,S*)-*iPr*-pybox)(Me)Br follows, and recombination with ind· produces Ni^{III}((*S,S*)-*iPr*-pybox)(Me)(ind)Br;

The Ni^{III} pathway: Oxidation by ind-Br proceeds to completion with Ni^{III}((*S,S*)-*iPr*-pybox)(ind)Br₂ being formed; subsequent methylation produces Ni^{III}((*S,S*)-*iPr*-pybox)(Me)(ind)Br.

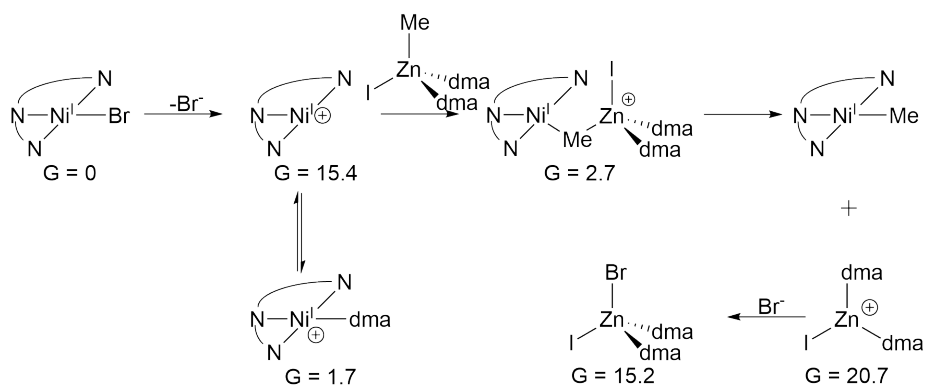
These three pathways are shown in Scheme 5.5.

The first branching point is the first step: Ni^I((*S,S*)-*iPr*-pybox)Br may either undergo methylation as in the Ni^I pathway, or one-electron oxidation by ind-Br as in the Ni^{II} and Ni^{III} pathways. Methylation of Ni^I((*S,S*)-*iPr*-pybox)Br to Ni^I((*S,S*)-*iPr*-pybox)Me is thermodynamically uphill by 15.2 kcal/mol. Unfortunately, we were unable to find any transition states for the concerted transfer of the methyl group from MeZnI(dma)₂ to any Ni^I species. However, we can consider a dissociative mechanism whereby the bromine on Ni^I((*S,S*)-*iPr*-pybox)Br is exchanged for a methyl group by the successive steps of Br⁻ dissociation, MeZnI(dma)₂ association, and ZnI(dma)₂⁺ dissociation (Scheme 5.6). Since each ligand association/disassociation step is expected to have minimal barriers if any, we can therefore gain an upper bound for the Ni^I methylation barrier by simply calculating the relative energies of each intermediate in Scheme 5.6. The results of our analysis shows that the overall barrier for the methylation of Ni^I((*S,S*)-*iPr*-pybox)Br to Ni^I((*S,S*)-*iPr*-pybox)Me is between 15.2 and 20.7 kcal/mol.

The Ni^{II} and Ni^{III} pathways, by contrast, begin with the oxidation of Ni^I((*S,S*)-*iPr*-pybox)Br

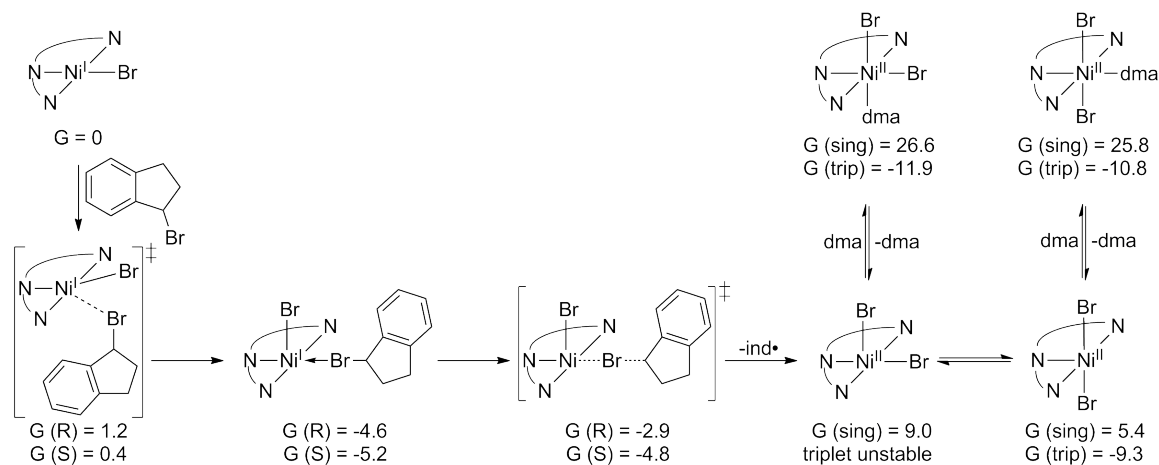


Scheme 5.5. Three potential pathways for the methylation and oxidation of $\text{Ni}^{\text{I}}((S,S)\text{-}i\text{Pr-pybox})\text{Br}$ to $\text{Ni}^{\text{III}}((S,S)\text{-}i\text{Pr-pybox})(\text{Me})(\text{ind})\text{Br}$. Red denotes the Ni^{I} pathway, green the Ni^{II} pathway, and blue the Ni^{III} pathway. Open coordination sites may be occupied by dma solvent.



Scheme 5.6. The dissociative pathway for the methylation of $\text{Ni}^{\text{I}}((S,S)\text{-}i\text{Pr-pybox})\text{Br}$ to $\text{Ni}^{\text{I}}((S,S)\text{-}i\text{Pr-pybox})\text{Me}$, as part of the Ni^{I} pathway in Scheme 5.5. The transition state barriers for each associative/dissociative step is expected to be minimal, if existent. Hence, the overall barrier to methylation by this pathway is 20.7 kcal/mol. All numbers are in kcal/mol and relative to $\text{Ni}^{\text{I}}((S,S)\text{-}i\text{Pr-pybox})\text{Br}$.

by ind-Br to $\text{Ni}^{\text{II}}((S,S)\text{-}i\text{Pr-pybox})\text{Br}_2$ and ind \cdot . This oxidation most likely proceeds through an inner sphere route that begins with coordination of ind-Br to the Ni center. Our results are shown in Scheme 5.7. Initial coordination of (*R*)- and (*S*)-1-bromoindane with $\text{Ni}^{\text{I}}((S,S)\text{-}i\text{Pr-pybox})\text{Br}$ produces an adduct $\text{Ni}^{\text{I}}((S,S)\text{-}i\text{Pr-pybox})(\text{Br})(\text{Br-ind})$ that is favorable at -4.6 and -5.2 kcal/mol relative to the initial Ni^{I} species, respectively. Loss of ind \cdot then results in $\text{Ni}^{\text{II}}((S,S)\text{-}i\text{Pr-pybox})\text{Br}_2$, whose triplet energy is -9.3 kcal/mol relative to the initial Ni^{I} species. The coordination of a DMA solvent molecule further lowers the triplet energy to -11.9 kcal/mol relative to the initial Ni^{I} species. The transition state barriers to ind-Br coordination and ind \cdot dissociation are indeed quite minimal at less than 1.7 kcal/mol, supporting our assumptions about the Ni^{I} methylation pathway. Since Ni^{I} methylation as *per* the Ni^{I} pathway is uphill thermodynamically by 15.2 kcal/mol, and Ni^{I} oxidation as *per* the Ni^{II} and Ni^{III} pathways is downhill by 11.9 kcal/mol with a maximum barrier of 1.2 kcal/mol, we conclude that the Ni^{II} and Ni^{III} pathways for $\text{Ni}^{\text{I}}((S,S)\text{-}i\text{Pr-pybox})\text{Br}$ methylation and oxidation are much more likely than the Ni^{I} pathway, which was the only pathway investigated by Lin *et al.*



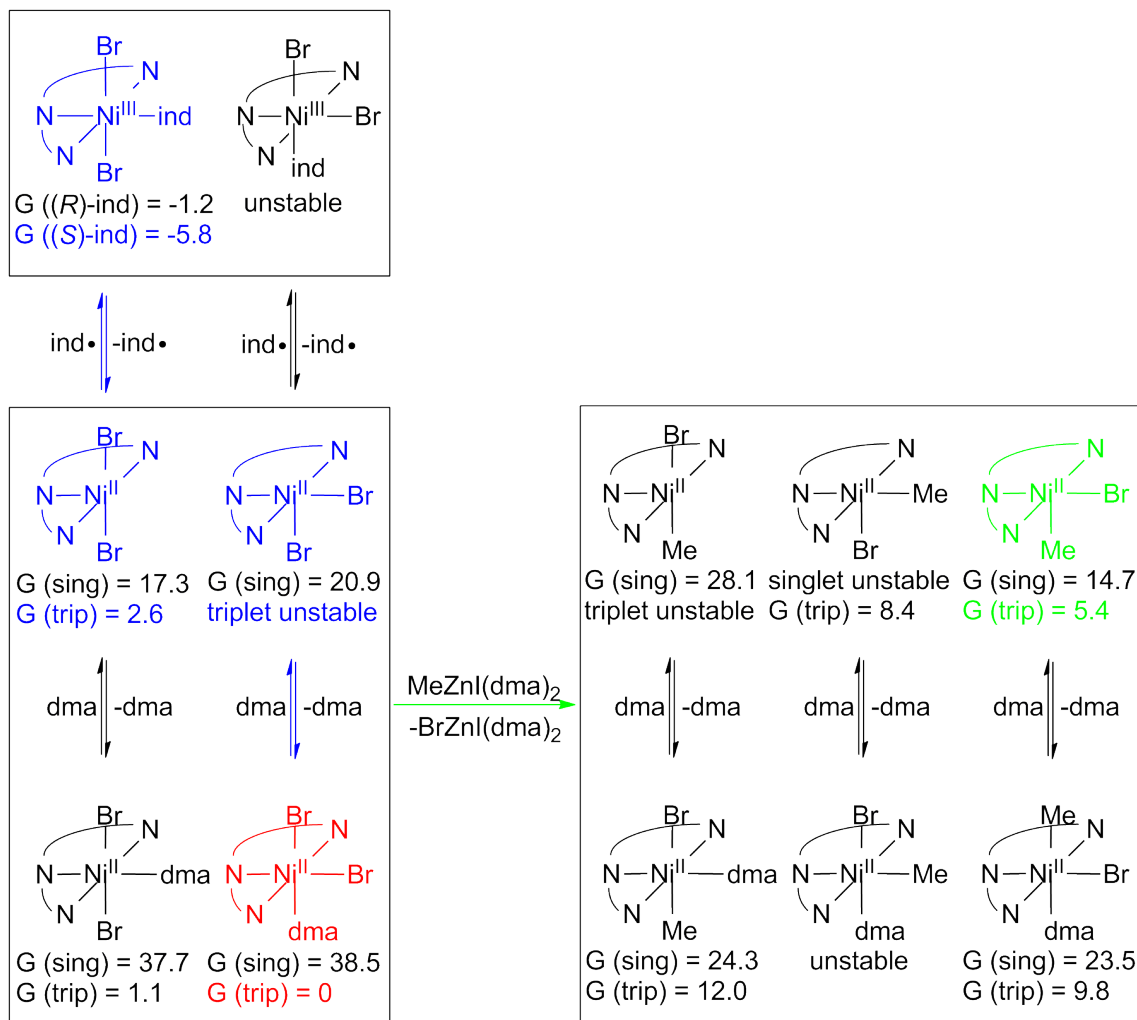
Scheme 5.7. The oxidation of $\text{Ni}^{\text{I}}((S,S)\text{-}i\text{Pr-pybox})\text{Br}$ by ind-Br to $\text{Ni}^{\text{II}}((S,S)\text{-}i\text{Pr-pybox})\text{Br}_2$ and ind \cdot , as part of the Ni^{II} and Ni^{III} pathways in Scheme 5.5. The transition state barrier for the coordination of DMA to $\text{Ni}^{\text{II}}((S,S)\text{-}i\text{Pr-pybox})\text{Br}_2$ is expected to be minimal, if existent. Hence, the overall barrier to oxidation by this pathway is 1.2 kcal/mol for (*R*)-1-bromoindane and 0.4 kcal/mol for (*S*)-1-bromoindane. All numbers are in kcal/mol and relative to $\text{Ni}^{\text{I}}((S,S)\text{-}i\text{Pr-pybox})\text{Br}$.

The second branching point is the subsequent reaction of $\text{Ni}^{\text{II}}((S,S)\text{-}i\text{Pr-pybox})\text{Br}_2(\text{dma})$, which can either undergo methylation to $\text{Ni}^{\text{II}}((S,S)\text{-}i\text{Pr-pybox})(\text{Me})\text{Br}$ as in the Ni^{II} pathway, or recombine with ind \cdot to form $\text{Ni}^{\text{III}}((S,S)\text{-}i\text{Pr-pybox})\text{Br}_2(\text{ind})$ as in the Ni^{III} pathway. Scheme 5.8 shows a comparison of the essential features of the two pathways, whereas Scheme 5.11 is an unabridged diagram of the Ni^{II} pathway. Methylation of $\text{Ni}^{\text{II}}((S,S)\text{-}i\text{Pr-pybox})\text{Br}_2(\text{dma})$ to $\text{Ni}^{\text{II}}((S,S)\text{-}i\text{Pr-pybox})(\text{Me})\text{Br}$ as in the Ni^{II} pathway is uphill by 5.4 kcal/mol. By contrast, recombination with ind \cdot to form $\text{Ni}^{\text{III}}((S,S)\text{-}i\text{Pr-pybox})\text{Br}_2(\text{ind})$ as in the Ni^{III} pathway is downhill by

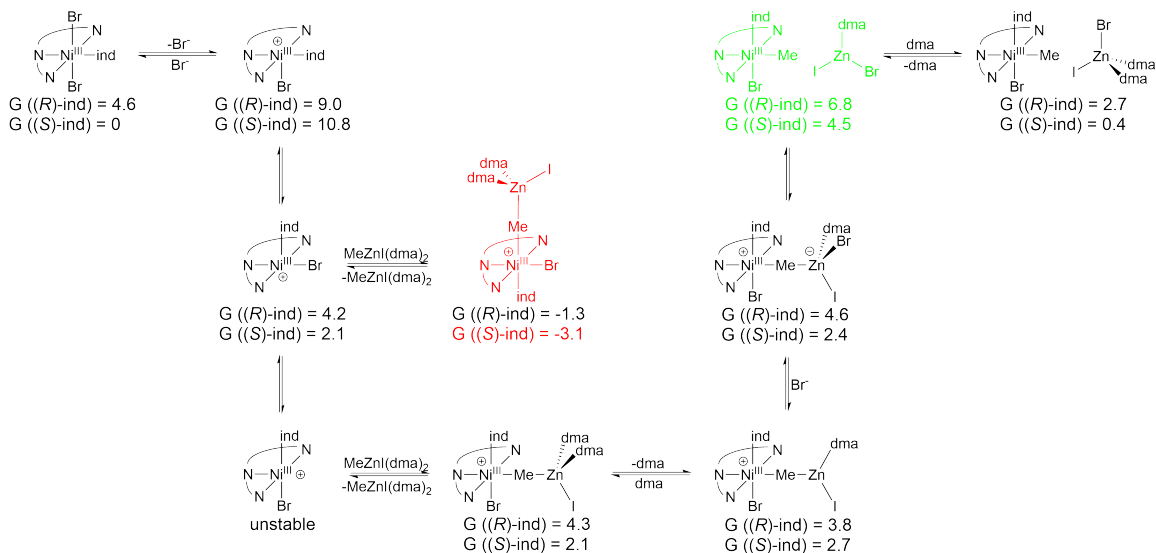
1.2 or 5.8 kcal/mol, depending on whether the indanyl ligand attaches in an (*R*) or (*S*) configuration, respectively. Since the dissociation of DMA from $\text{Ni}^{\text{II}}((S,S)\text{-}i\text{Pr-pybox})\text{Br}_2(\text{dma})$ is uphill by 2.6 kcal/mol, and the addition of $\text{ind}\cdot$ is expected to have minimal barrier, we can conclude that the overall barrier of the reaction of $\text{Ni}^{\text{II}}((S,S)\text{-}i\text{Pr-pybox})\text{Br}_2(\text{dma})$ and $\text{ind}\cdot$ is likely lower than that of $\text{Ni}^{\text{II}}((S,S)\text{-}i\text{Pr-pybox})\text{Br}_2(\text{dma})$ and $\text{MeZnI}(\text{dma})_2$, and hence that the Ni^{III} pathway is preferred over the Ni^{II} pathway.

The Ni^{I} , Ni^{II} , and Ni^{III} pathways all converge to $\text{Ni}^{\text{III}}((S,S)\text{-}i\text{Pr-pybox})(\text{Me})(\text{ind})\text{Br}$ in the final step. For the Ni^{III} pathway, this involves the methylation of the $\text{Ni}^{\text{III}}((S,S)\text{-}i\text{Pr-pybox})\text{Br}_2(\text{ind})$ formed as described in the previous Scheme 5.8. As in the Ni^{I} methylation case, we were unable to find any transition states for the concerted transfer of the methyl group from $\text{MeZnI}(\text{dma})_2$ to any Ni^{III} species. Hence we again considered a dissociative mechanism whereby a bromine on $\text{Ni}^{\text{III}}((S,S)\text{-}i\text{Pr-pybox})\text{Br}_2(\text{ind})$ is exchanged for a methyl group by the successive steps of Br^- dissociation, $\text{MeZnI}(\text{dma})_2$ association, and $\text{ZnI}(\text{dma})_2^+$ dissociation, assuming that our barriers are minimal and thus estimating our overall methylation barriers using thermodynamic energies only. A comprehensive accounting of all species studied for this Ni^{III} methylation reaction is given in Scheme 5.12 in Section 5.7.

Scheme 5.9 shows the essential features of the mechanism of Ni^{III} methylation. The initial $\text{Ni}^{\text{III}}((S,S)\text{-}i\text{Pr-pybox})\text{Br}_2(\text{ind})$ may lose a bromo ligand, resulting in a five-coordinate cationic species $[\text{Ni}^{\text{III}}((S,S)\text{-}i\text{Pr-pybox})\text{Br}(\text{ind})]^+$ that may exist in three separate but interchangeable geometric conformations. Each conformation may then trap an equivalent of $\text{MeZnI}(\text{dma})_2$, with the species $[\text{Ni}^{\text{III}}((S,S)\text{-}i\text{Pr-pybox})\text{Br}^{\text{eq}}((S)\text{-ind})^{\text{ax}}\text{-Me}^{\text{ax}}\text{-ZnI}(\text{dma})_2]^+$ the most favorable at -3.1 kcal/mol relative to the starting $\text{Ni}^{\text{III}}((S,S)\text{-}i\text{Pr-pybox})\text{Br}_2((S)\text{-ind})$. However, it is the isomer $[\text{Ni}^{\text{III}}((S,S)\text{-}i\text{Pr-pybox})\text{Br}^{\text{ax}}(\text{ind})^{\text{ax}}\text{-Me}^{\text{eq}}\text{-ZnI}(\text{dma})_2]^+$ that eventually leads to the lowest $\text{Ni}^{\text{III}}(\text{Me})(\text{ind})\text{Br}$ species, $\text{Ni}^{\text{III}}((S,S)\text{-}i\text{Pr-pybox})\text{Br}^{\text{ax}}(\text{ind})^{\text{ax}}\text{Me}^{\text{eq}}$. Dissociation of $\text{ZnBrI}(\text{dma})$ from $\text{Ni}^{\text{III}}((S,S)\text{-}i\text{Pr-pybox})\text{Br}^{\text{ax}}(\text{ind})^{\text{ax}}\text{-Me}^{\text{eq}}\text{-ZnBrI}(\text{dma})$ leads to $[\text{Ni}^{\text{III}}((S,S)\text{-}i\text{Pr-pybox})\text{-Br}^{\text{ax}}(\text{ind})^{\text{ax}}\text{Me}^{\text{eq}}]$ and is 6.8 or 4.5 kcal/mol uphill from the starting $\text{Ni}^{\text{III}}((S,S)\text{-}i\text{Pr-pybox})\text{Br}_2((S)\text{-ind})$, but coordination of $\text{ZnBrI}(\text{dma})$ with solvent back to $\text{ZnBrI}(\text{dma})_2$ drives this reaction forward. As we have assumed that association and dissociation barriers are minimal for these reactions, the overall barrier for the methylation of $\text{Ni}^{\text{III}}((S,S)\text{-}i\text{Pr-pybox})\text{Br}_2((S)\text{-ind})$ is approximately the difference between the highest point ($[\text{Ni}^{\text{III}}((S,S)\text{-}i\text{Pr-pybox})\text{Br}^{\text{ax}}(\text{ind})^{\text{ax}}\text{Me}^{\text{eq}} + \text{ZnBrI}(\text{dma})$) and the lowest point ($[\text{Ni}^{\text{III}}((S,S)\text{-}i\text{Pr-pybox})\text{Br}^{\text{eq}}((S)\text{-ind})^{\text{ax}}\text{-Me}^{\text{ax}}\text{-ZnI}(\text{dma})_2]^+$), equal to 9.9 and 7.6 kcal/mol for the formation of $\text{Ni}^{\text{III}}((S,S)\text{-}i\text{Pr-pybox})\text{Br}^{\text{ax}}((R)\text{-ind})^{\text{ax}}\text{Me}^{\text{eq}}$ and $\text{Ni}^{\text{III}}((S,S)\text{-}i\text{Pr-pybox})\text{Br}^{\text{ax}}((S)\text{-ind})^{\text{ax}}\text{Me}^{\text{eq}}$, respectively.



Scheme 5.8. $\text{Ni}^{\text{II}}((S,S)\text{-}i\text{Pr-pybox})\text{Br}_2$ and its subsequent methylation as part of the Ni^{II} pathway, or recombination with $\text{ind}\cdot$ as part of the Ni^{III} pathway. The lowest energy $\text{Ni}^{\text{II}}((S,S)\text{-}i\text{Pr-pybox})\text{MeBr}$ complex is 5.4 kcal/mol higher than the starting $\text{Ni}^{\text{II}}((S,S)\text{-}i\text{Pr-pybox})\text{Br}_2$, so the overall barrier for methylation is at least this much. By contrast, the transition state barrier for the coordination of $\text{ind}\cdot$ to $\text{Ni}^{\text{II}}((S,S)\text{-}i\text{Pr-pybox})\text{Br}_2$ is expected to be minimal, if existent. Hence, the overall barrier to $\text{ind}\cdot$ recombination is 2.6 kcal/mol, and the Ni^{III} pathway is thus more likely to occur. All numbers are in kcal/mol and relative to $\text{Ni}^{\text{II}}((S,S)\text{-}i\text{Pr-pybox})\text{Br}_2$. Red denotes the starting $\text{Ni}^{\text{II}}((S,S)\text{-}i\text{Pr-pybox})\text{Br}_2(\text{dma})$ complex, green the Ni^{II} pathway, and blue the Ni^{III} pathway. Note that indanyl recombination is reversible, so that $\text{Ni}^{\text{III}}((R)\text{-}i\text{Pr-pybox})\text{Br}_2((S)\text{-ind})$ and $\text{Ni}^{\text{III}}((S,S)\text{-}i\text{Pr-pybox})\text{Br}_2((S)\text{-ind})$ can interconvert.



Scheme 5.9. The methylation of $\text{Ni}^{\text{III}}((S,S)\text{-}i\text{Pr-pybox})\text{Br}_2((S)\text{-ind})$ to produce $\text{Ni}^{\text{III}}((S,S)\text{-}i\text{Pr-pybox})(\text{Br})(\text{ind})\text{Me}$. The reaction initially proceeds to $[\text{Ni}^{\text{III}}((S,S)\text{-}i\text{Pr-pybox})\text{Br}^{\text{eq}}((S)\text{-ind})^{\text{ax}}\text{-Me}^{\text{ax}}\text{-ZnI}(\text{dma})_2]^+$, a thermodynamic sink, and must increase in energy in order to reach the $\text{Ni}^{\text{III}}((S,S)\text{-}i\text{Pr-pybox})\text{Br}^{\text{ax}}(\text{ind})^{\text{ax}}\text{Me}^{\text{eq}}$ product. All numbers are in kcal/mol and relative to $\text{Ni}^{\text{III}}((S,S)\text{-}i\text{Pr-pybox})\text{Br}_2((S)\text{-ind})$. Red denotes the lowest point and thermodynamic sink, $[\text{Ni}^{\text{III}}((S,S)\text{-}i\text{Pr-pybox})\text{Br}^{\text{eq}}((S)\text{-ind})^{\text{ax}}\text{-Me}^{\text{ax}}\text{-ZnI}(\text{dma})_2]^+$; and green the highest point, $\text{Ni}^{\text{III}}((S,S)\text{-}i\text{Pr-pybox})\text{Br}^{\text{ax}}(\text{ind})^{\text{ax}}\text{Me}^{\text{eq}} + \text{ZnBrI}(\text{dma})$.

5.4.4 Mechanism for reductive elimination

After the formation of $\text{Ni}^{\text{III}}((S,S)\text{-}i\text{Pr-pybox})(\text{Me})(\text{ind})\text{Br}$, the final step to closing the catalytic cycle is the reductive elimination of ind-Me and the reformation of $\text{Ni}^{\text{I}}((S,S)\text{-}i\text{Pr-pybox})\text{Br}$ (Scheme 5.3, bottom half of cycle). In the computational work of Lin et al., only the reductive elimination of ind-Me from $\text{Ni}^{\text{III}}((S,S)\text{-}i\text{Pr-pybox})(\text{Me})^{\text{eq}}(\text{ind})^{\text{ax}}\text{Br}^{\text{ax}}$ was considered. However, we believe that this is not the only possible pathway for the reductive elimination of ind-Me . Specifically:

1. Reductive elimination may proceed from either $\text{Ni}^{\text{III}}((S,S)\text{-}i\text{Pr-pybox})(\text{Me})^{\text{ax}}(\text{ind})^{\text{eq}}\text{Br}^{\text{ax}}$ or $\text{Ni}^{\text{III}}((S,S)\text{-}i\text{Pr-pybox})(\text{Me})^{\text{eq}}(\text{ind})^{\text{ax}}\text{Br}^{\text{ax}}$;
2. It is possible for the bromo ligand to be lost, resulting in five-coordinate cationic $[\text{Ni}^{\text{III}}((S,S)\text{-}i\text{Pr-pybox})(\text{Me})(\text{ind})]^+$ species that may also reductively eliminate;
3. It is possible for the five coordinate cationic species to be stabilized by a solvent ligand, resulting in the six-coordinate cationic $[\text{Ni}^{\text{III}}((S,S)\text{-}i\text{Pr-pybox})(\text{Me})(\text{ind})\text{dma}]^+$ species that may also reductively eliminate;
4. It is also possible for the five coordinate cationic species to coordinate to zinc, forming an adduct $\text{Ni}^{\text{III}}((S,S)\text{-}i\text{Pr-pybox})(\text{Me})(\text{ind})\text{-Br-[Zn]}$ that may also reductively eliminate.

For the last possibility, the only transition states found that contained the Ni–Br–Zn moiety were the geometric isomers of $[\text{Ni}^{\text{III}}((S,S)\text{-}i\text{Pr-pybox})(\text{Me})(\text{ind})\text{-Br-ZnBr}_2\text{I}]^-$. In all other cases, the Br–[Zn] moiety dissociated from the Ni during geometry optimization.

Figure 5.4 shows all the transition states that have been found, and their energies relative to $[\text{Ni}^{\text{III}}((S,S)\text{-}i\text{Pr-pybox})\text{Br}^{\text{eq}}((S)\text{-ind})^{\text{ax}}\text{-Me}^{\text{ax}}\text{-ZnI}(\text{dma})_2]^+$, the lowest energy state of the catalyst. A reaction scheme showing the pathways to all transition states is given in Section 5.7 as Scheme 5.13. The lowest energy transition state that produces (*R*)-1-methylindane is $[\text{Ni}^{\text{III}}((S,S)\text{-}i\text{Pr-pybox})(\text{Me})^{\text{ax}}((R)\text{-ind})^{\text{eq}}\text{-Br}^{\text{ax}}\text{-ZnBr}_2\text{I}]^-$, with an overall barrier of 18.6 kcal/mol, and the lowest energy transition state that produces (*S*)-1-methylindane is $[\text{Ni}^{\text{III}}((S,S)\text{-}i\text{Pr-pybox})(\text{Me})^{\text{ax}}((S)\text{-ind})^{\text{eq}}]^+$, with an overall barrier of 15.9 kcal/mol. Hence, the preference for (*S*)-1-methylindane is $\Delta\Delta G^\ddagger = 2.7$ kcal/mol, in line with experimentally determined enantiomeric excesses [15].

5.5 Discussion

5.5.1 Overall catalytic cycle

Figure 5.5 is a reaction coordinate diagram that summarizes our results for the investigation of the oxidation and methylation of $\text{Ni}^{\text{I}}((S,S)\text{-}i\text{Pr-pybox})\text{Br}$ to $\text{Ni}^{\text{III}}((S,S)\text{-}i\text{Pr-pybox})(\text{Me})(\text{ind})\text{Br}$, and the subsequent reductive elimination of ind–Me and reformation of $\text{Ni}^{\text{I}}((S,S)\text{-}i\text{Pr-pybox})\text{Br}$. All three pathways are shown and the Ni^{III} pathway is clearly the easiest. The lowest point and thermodynamic sink, $[\text{Ni}^{\text{III}}((S,S)\text{-}i\text{Pr-pybox})\text{Br}^{\text{eq}}((S)\text{-ind})^{\text{ax}}\text{-Me}^{\text{ax}}\text{-ZnI}(\text{dma})_2]^+$, is now considered the resting state, and all other free energies given are relative to it. The overall barrier is 18.6 and 15.9 kcal/mol for the formation of (*R*)-1-methylindane and (*S*)-1-methylindane, respectively.

5.5.2 Predictions for new ligands

Now that the mechanism of $\text{Ni}((S,S)\text{-}i\text{Pr-pybox})$ asymmetric Negishi coupling catalysis has been ascertained, it is useful to consider how modification of the $((S,S)\text{-}i\text{Pr-pybox})$ ligand may affect enantioselectivity. The most obvious point of modification is the R groups on the oxazoline moieties. However, the synthesis and mechanistic analysis of a multitude of R–pybox ligands would be expected to be costly and time-consuming. Hence, it is better to computationally examine a generalized mechanism of R–pybox catalysis that may be systematically and rapidly adapted for different R groups, for high-throughput screening of new R–pybox catalysts for asymmetric Negishi coupling.

A generalized catalytic mechanism for the $\text{Ni}(\text{R-pybox})$ complexes is given in Scheme 5.10. The starting complex $\text{Ni}^{\text{I}}(\text{R-pybox})\text{Br}$, **G**, is oxidized and methylated to $\text{Ni}^{\text{III}}(\text{R-pybox})(\text{Me})(\text{ind})\text{Br}$ (not shown). The $\text{Ni}^{\text{III}}(\text{R-pybox})(\text{Me})(\text{ind})\text{Br}$ species, which can exist in three geometric isomers

Figure 5.4. Transition states for the reductive elimination of 1-methylindane from various Ni^{III}-((*S,S*)-*i*Pr-pybox)(Me)ind species. All numbers are in kcal/mol and relative to [Ni^{III}((*S,S*)-*i*Pr-pybox)-Br^{eq}((*S*)-ind)^{ax}-Me^{ax}-ZnI(dma)₂]⁺. The lowest transition states for the formation of (*R*)- and (*S*)-1-methylindane are highlighted in green and blue, respectively.

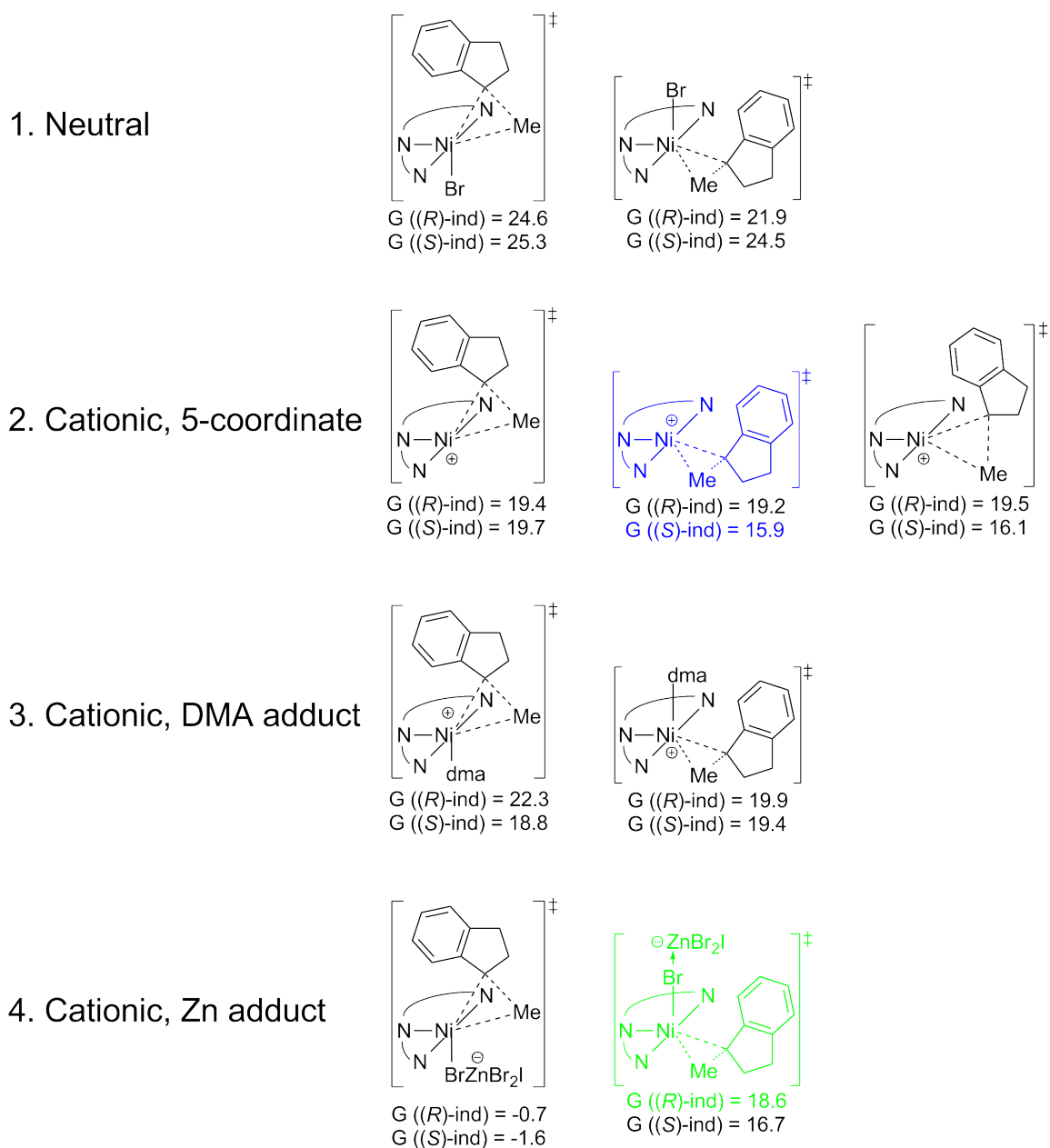
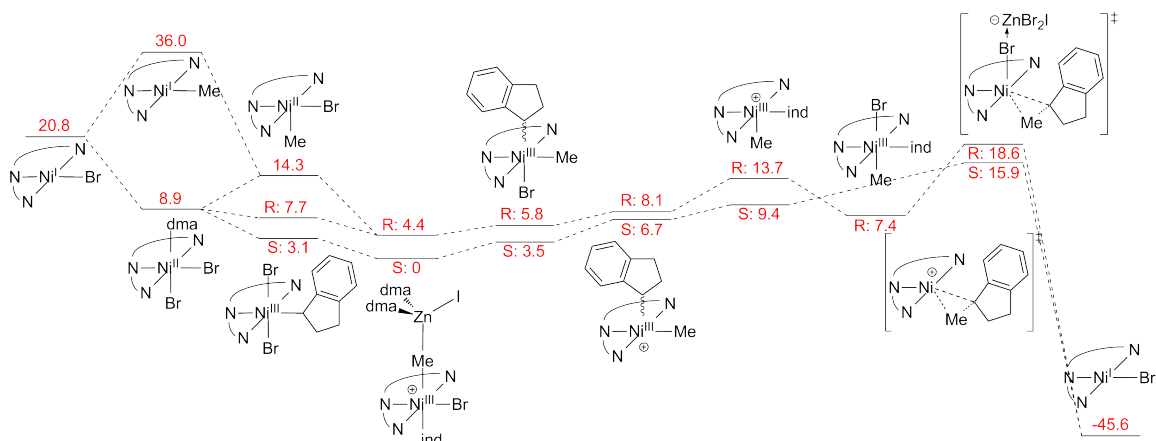


Figure 5.5. Reaction coordinate diagram of the entire catalytic cycle for the coupling of ind–Br and MeZnI to form ind–Me. All numbers are in kcal/mol and relative to $[\text{Ni}^{\text{III}}((S,S)\text{-}i\text{Pr}\text{-pybox})\text{Br}^{\text{eq}}\text{-}((S)\text{-ind})^{\text{ax}}\text{-Me}^{\text{ax}}\text{-ZnI}(\text{dma})_2]^+$.

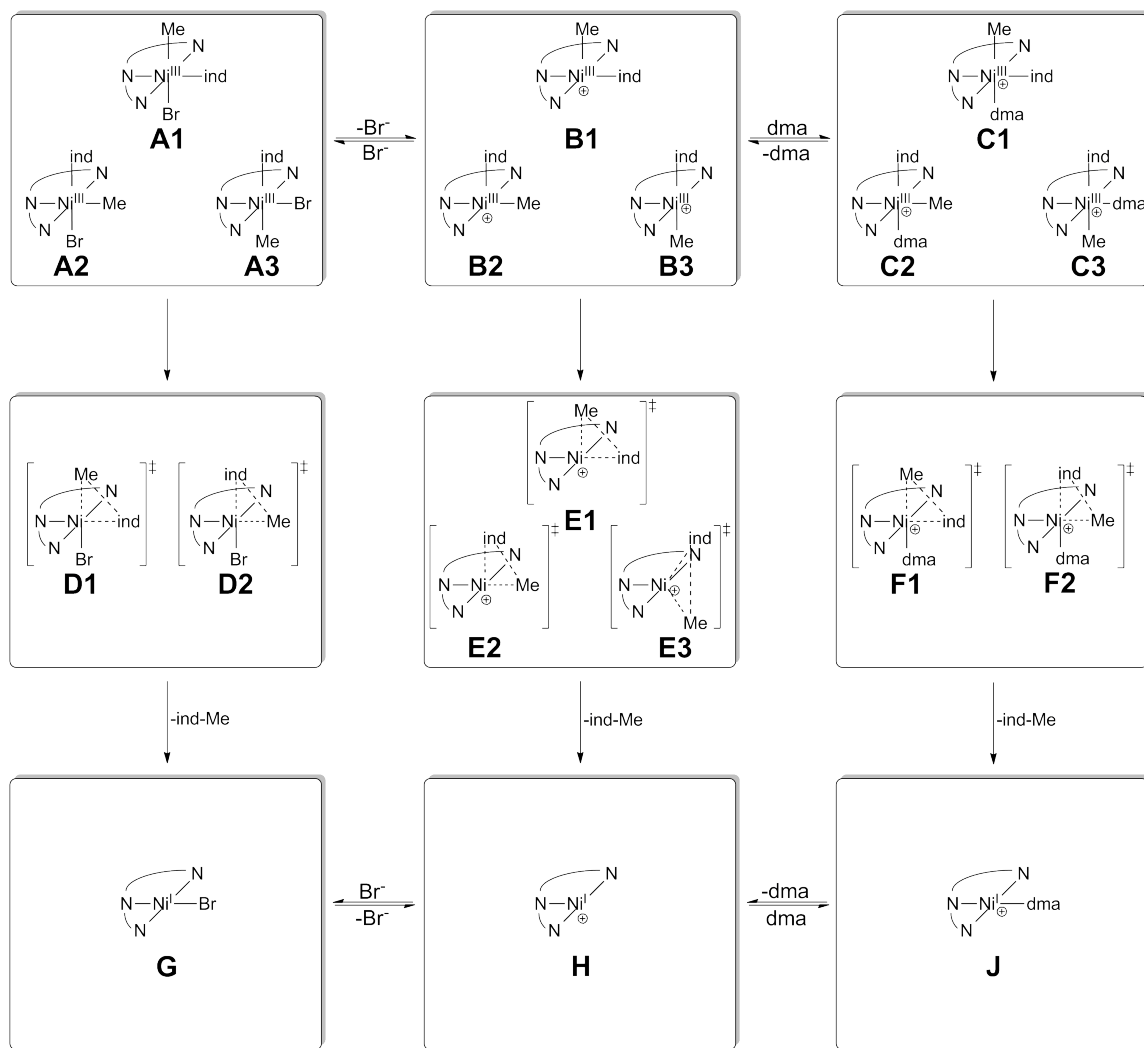


A1, **A2**, and **A3**, may lose Br^- to form the five coordinate cationic $[\text{Ni}^{\text{III}}(\text{R}\text{-pybox})(\text{Me})\text{ind}]^+$ species **B1**, **B2**, and **B3**, respectively. A DMA solvent molecule may then coordinate to the open coordination site to form cationic $[\text{Ni}^{\text{III}}(\text{R}\text{-pybox})(\text{Me})(\text{ind})\text{dma}]^+$ species **C1**, **C2**, and **C3**, respectively. Neutral **A1** and **A2** (but not **A3**) may also undergo reductive elimination through the transition states **D1** and **D2**, respectively, to release methylindane and reform the starting complex **G**. Likewise, **B1**, **B2**, and **B3** may undergo reductive elimination through **E1**, **E2**, and **E3**, respectively, to release methylindane and form cationic $[\text{Ni}^{\text{I}}(\text{R}\text{-pybox})]^+$, **H**, which can regain the bromide to reform the starting complex **G**. Finally, cationic **C1** and **C2** (but not **C3**) may undergo reductive elimination through the transition states **F1** and **F2**, respectively, to release methylindane and cationic $[\text{Ni}^{\text{I}}(\text{R}\text{-pybox})\text{dma}]^+$, **J**, which can replace its dma ligand with a bromide to reform the starting complex **G**.

In order to rapidly calculate the enantioselectivity of $\text{Ni}(\text{R}\text{-pybox})$ catalysts containing different R groups, we simply need to find the transition states **D**, **E**, and **F**. (In our future analyses, we will also consider Zn adducts as well, but that is not included in this study.) For our demonstration, we have selected potential R groups to be adamantyl (Ad), cyclohexyl (Cy), methyl (Me), phenyl (Ph), (*R*)-*sec*-butyl (*(R)*-*s*Bu), (*S*)-*sec*-butyl (*(S)*-*s*Bu), *tert*-butyl (*t*Bu), and 2-phenylethyl ($\text{C}_2\text{H}_4\text{Ph}$). In addition, we also considered the a variant pyridine bis(indenoxazoline) ligand with fused indane rings, which we term pybindox. These are shown in Figure 5.6.

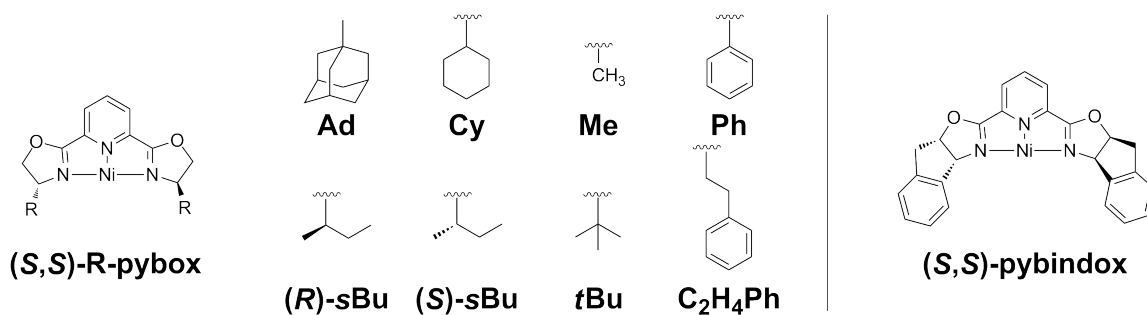
Our results are given in Table 5.3. A complete collection of all calculated intermediate and transition state energies is given in Tables 5.4 through 5.6 in Section 5.7.

Despite the variety of different R groups investigated, several universal characteristics may be observed from the data in Tables 5.3 through 5.6. In every case, the lowest energy intermediate was a neutral **A** species, usually the **A2** isomer. However, the lowest transition states are of type **E**,



Scheme 5.10. A generalized catalytic mechanism that Ni(R-pybox) complexes undergo in Negishi coupling. This scheme is used to rapidly calculate the predicted enantioselectivity of a variety of complexes related to the original Ni(*i*Pr-pybox) system.

Figure 5.6. Modified ligands studied which, when complexed to Ni, may allow for different enantioselective properties as compared to the original (*i*Pr-pybox) ligand.



R	[Ni ^{III} (L)(Me--ind)Br] [‡] (D)			[Ni ^{III} (L)(Me--ind)] ^{+‡} (E)			[Ni ^{III} (L)(Me--ind)dma] ^{+‡} (F)		
	minimum ΔG^\ddagger		$\Delta\Delta G^\ddagger$	minimum ΔG^\ddagger		$\Delta\Delta G^\ddagger$	minimum ΔG^\ddagger		$\Delta\Delta G^\ddagger$
	(<i>R</i>)	(<i>S</i>)		(<i>R</i>)	(<i>S</i>)		(<i>R</i>)	(<i>S</i>)	
<i>i</i> Pr	18.4	17.3	1.1	15.7	12.4	3.3	16.4	15.3	1.1
Ad	19.1	19.6	-0.5	14.9	16.4	-1.5	19.3	17.2	2.1
Cy	28.5	28.9	-0.3	20.3	18.8	1.5	N/A	30.9	N/A
Me	20.3	18.9	1.4	15.2	13.8	1.4	N/A	19.2	N/A
Ph	17.7	16.2	1.6	14.9	12.6	2.3	17.1	15.8	1.3
(<i>R</i>)- <i>s</i> Bu	18.3	15.7	2.6	12.5	12.1	0.5	N/A	N/A	N/A
(<i>S</i>)- <i>s</i> Bu	18.1	17.0	1.2	15.4	13.5	1.9	N/A	16.5	N/A
<i>t</i> Bu	18.9	18.9	0.0	16.1	16.7	-0.6	19.5	18.3	1.2
C ₂ H ₄ Ph	17.5	19.4	-1.9	12.8	10.7	2.1	N/A	14.7	N/A
pybindox	20.5	18.9	1.7	13.7	13.3	0.3	17.3	15.0	2.3

Table 5.3. Comparison of activation energies for transition states of type **D**, **E**, and **F** for various Ni(R-pybox) catalysts. The Ni(*i*Pr-pybox) data is also given here for comparison. For each transition state type, only the energy of the lowest geometric isomer is reported. For all R groups, cationic five-coordinate transition states (**E**) were most favored. The (*R*)-(*S*) $\Delta\Delta G^\ddagger$ value is also calculated for each transition state type and (R-pybox) ligand. All numbers are in kcal/mol. Energies given are relative to the lowest calculated type **A** neutral Ni^{III}(R-pybox)(Me)(ind)Br complex. Numbers in blue are the lowest energy transition states for the production of (*R*)-1-methylindane, whereas numbers in red are the lowest energy transition states for the production of (*S*)-1-methylindane. Numbers in green are the final $\Delta\Delta G^\ddagger$ values for each R. (L) is ((*S*, *S*)-R-pybox).

although the particular isomer (i.e. **E1**, **E2**, or **E3**) may vary. The enantioselectivity as measured by $\Delta\Delta G^\ddagger$ varies from -1.5 to 2.3 kcal/mol, in all cases inferior to the original Ni(*i*Pr-pybox)'s $\Delta\Delta G^\ddagger$ value of 2.7 kcal/mol. In our future studies, we will seek to gain more accurate $\Delta\Delta G^\ddagger$ values for our existing R groups by also considering Zn adduct formation, as we have done for Ni(*i*Pr-pybox); and broaden our search to examine more R groups.

5.6 Conclusions

In this chapter, we have computationally studied the mechanism of the Ni(*i*Pr-pybox) system, which is a enantioselective and stereoconvergent Negishi C-C coupling catalyst. Our results support existing experimental and theoretical evidence that the mechanism proceeds through a Ni^I-Ni^{III} cycle, with the stereochemistry of the initial ind-Br destroyed by homolytic cleavage of the C-Br bond. We found that Ni^I((*S*, *S*)-*i*Pr-pybox)Br is initially oxidized by ind-Br, and then methylated to form Ni^{III}((*S*, *S*)-*i*Pr-pybox)(Me)(ind)Br, which can form an adduct with Zn to result in the resting state [Ni^{III}((*S*, *S*)-*i*Pr-pybox)Br^{eq}((*S*)-ind)^{ax}-Me^{ax}-ZnI(dma)₂]⁺. Reductive elimination then proceeds through either [Ni^{III}((*S*, *S*)-*i*Pr-pybox)(Me)^{ax}((*R*)-ind)^{eq}-Br^{ax}-ZnBr₂I]⁻ at an overall barrier of 18.6 kcal/mol to form (*R*)-1-methylindane, or [Ni^{III}((*S*, *S*)-*i*Pr-pybox)(Me)^{ax}((*S*)-ind)^{eq}]⁺ at an overall barrier of 15.9 kcal/mol to form (*S*)-1-methylindane, with an enantioselectivity of $\Delta\Delta G^\ddagger = 2.7$ kcal/mol preference for forming the (*S*) enantiomer. These results

are also in line with experimental evidence.

In addition, we formulated a systematic approach that allows us to rapidly study related Ni(R-pybox) systems, where R is Ad, Cy, Me, Ph, (*R*)-*s*Bu, (*S*)-*s*Bu, *t*Bu, or C₂H₄Ph, or the ligand is pybindox. For these cases, we have found [Ni^{III}(R-pybox)(Me)(ind)]⁺ (**E**) to be universally the lowest energy transition states for the production of either (*R*)- or (*S*)-1-methylindane. Our $\Delta\Delta G^\ddagger$ values measured range from -1.5 to 2.3 kcal/mol, which are not as good as the original Ni(*i*Pr-pybox). We are continuing to improve our screening system and broadening our scope to find new catalysts for efficient asymmetric and stereoconvergent catalysis for C-C coupling.

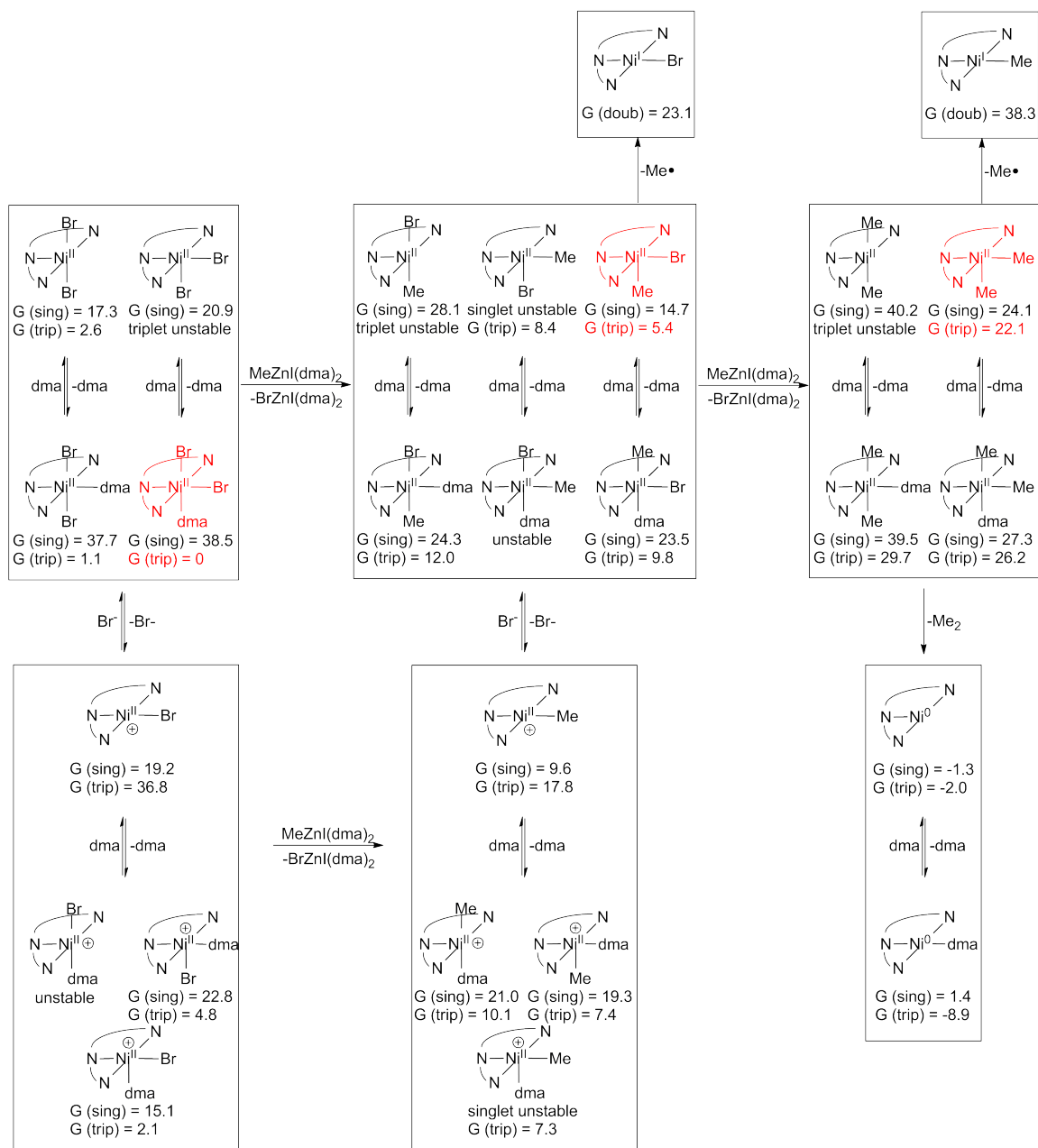
5.7 Supporting figures

Scheme 5.11 is an expanded diagram of the Ni^{II} pathway, whose essential features were presented in Scheme 5.8. Although methylation of Ni^{II}((*S,S*)-*i*Pr-pybox)Br₂ to Ni^{II}((*S,S*)-*i*Pr-pybox)(Me)Br is uphill by 5.4 kcal/mol, further methylation to Ni^{II}((*S,S*)-*i*Pr-pybox)Me₂ is uphill by an additional 16.7 kcal/mol. Reductive elimination of ethane is thermodynamically favorable, but the loss of methyl radical from either Ni^{II}((*S,S*)-*i*Pr-pybox)(Me)Br or Ni^{II}((*S,S*)-*i*Pr-pybox)Me₂ is very uphill. Hence, the overall barrier to ethane production is at least 22.1 kcal/mol, the energy of the lowest Ni^{II}((*S,S*)-*i*Pr-pybox)Me₂ species.

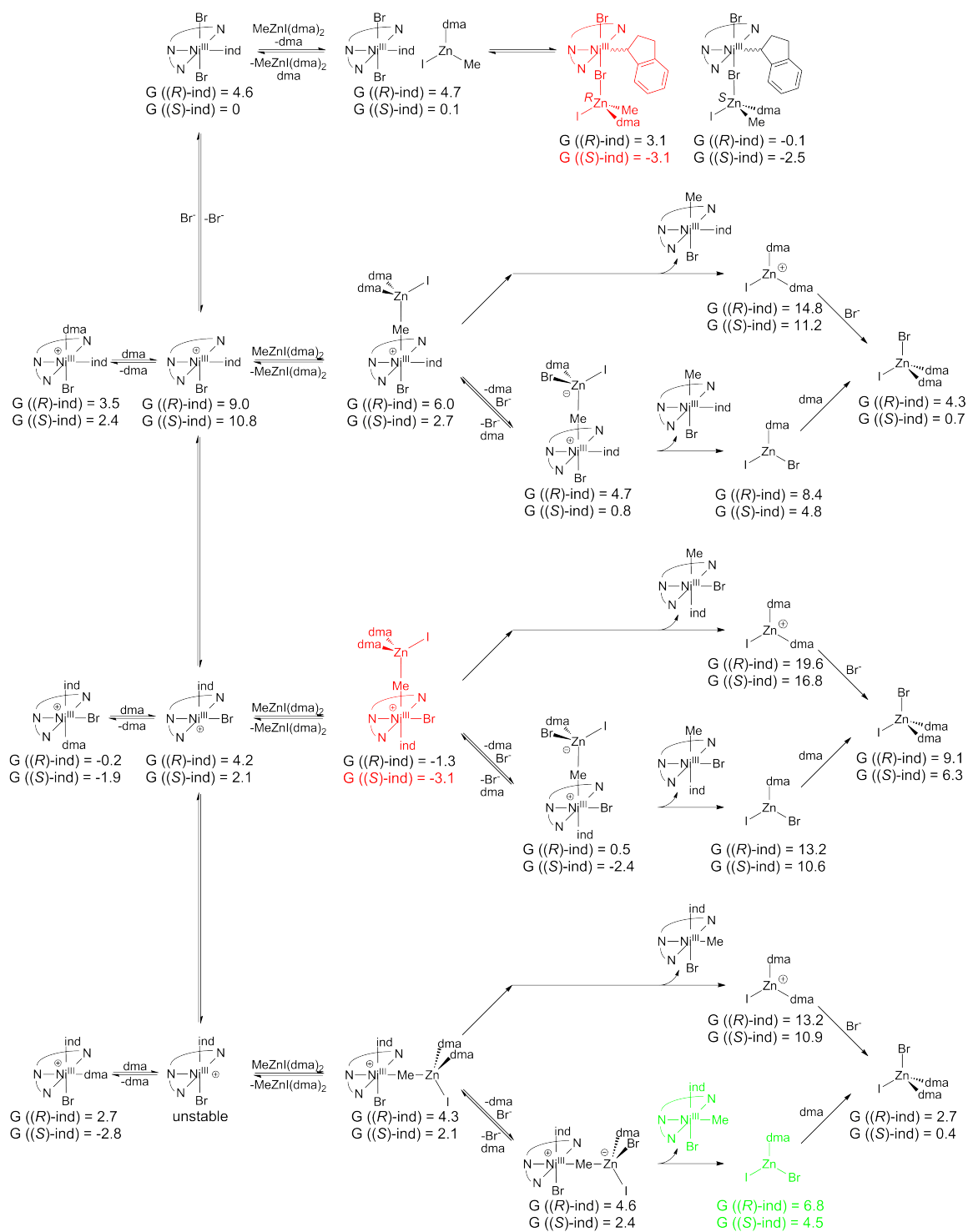
Scheme 5.12 is an expanded version of Scheme 5.9, showing the methylation of Ni^{III}((*S,S*)-*i*Pr-pybox)Br₂((*S*)-ind) to [Ni^{III}((*S,S*)-*i*Pr-pybox)Br(ind)Me], as well as all side reactions and isomers investigated.

Scheme 5.13 shows the reactions of Ni^{III}((*S,S*)-*i*Pr-pybox)(Br)(ind)Me that lead to ind-Me reductive elimination. (*R*)- and (*S*)-1-methylindane are produced in separate pathways, highlighted in red and blue, respectively. The overall barriers are 18.6 kcal/mol for the production of (*R*)-1-methylindane and 15.9 kcal/mol for production of (*S*)-1-methylindane, leading to a $\Delta\Delta G^\ddagger$ preference of 2.7 kcal/mol for the (*S*) isomer.

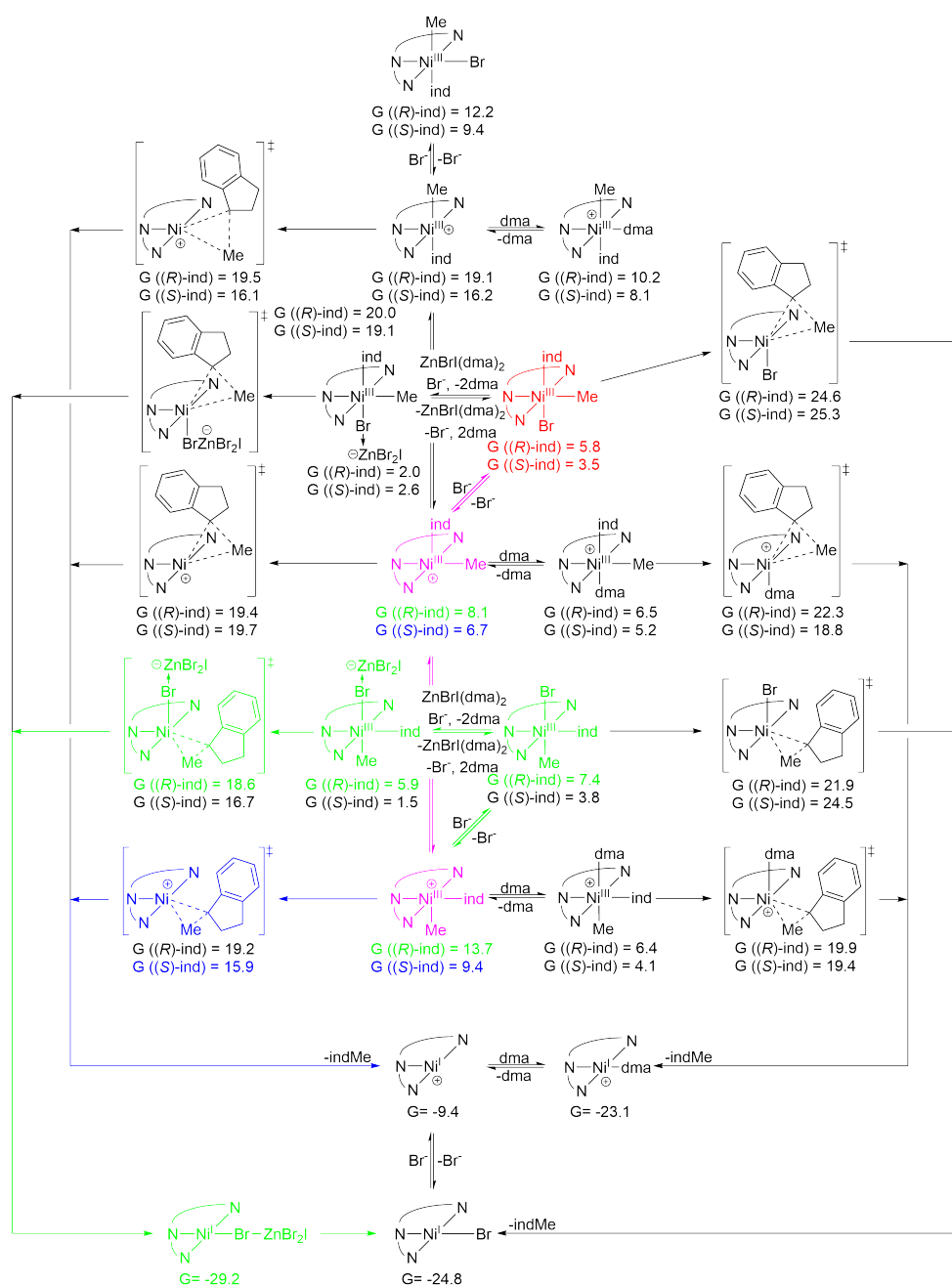
Tables 5.4 through 5.6 show the calculated energies of all transition states and intermediates **A** through **J** for the high-throughput screening of Ni(R-pybox) catalysts, where R is Ad, Cy, Me, Ph, (*R*)-*s*Bu, (*S*)-*s*Bu, *t*Bu, or C₂H₄Ph, or the ligand is pybindox. Specifically, Table 5.4 shows the neutral sequence **A** → **D** → **G**; Table 5.5 shows the cationic sequence **B** → **E** → **H**; and Table 5.6 shows the cationic sequence **C** → **F** → **J** (see Scheme 5.10). A future study will also include Ni-Br-Zn adducts as well.



Scheme 5.11. Expanded diagram of $\text{Ni}^{\text{II}}((S,S)\text{-}i\text{Pr-pybox})\text{Br}_2$ methylation as part of the Ni^{II} pathway. The lowest energy $\text{Ni}^{\text{II}}((S,S)\text{-}i\text{Pr-pybox})\text{MeBr}$ complex is 5.4 kcal/mol higher than the starting $\text{Ni}^{\text{II}}((S,S)\text{-}i\text{Pr-pybox})\text{Br}_2$, and the lowest energy $\text{Ni}^{\text{II}}((S,S)\text{-}i\text{Pr-pybox})\text{Me}_2$ complex is 22.1 kcal/mol higher than the starting $\text{Ni}^{\text{II}}((S,S)\text{-}i\text{Pr-pybox})\text{Br}_2$. All numbers are in kcal/mol and relative to $\text{Ni}^{\text{II}}((S,S)\text{-}i\text{Pr-pybox})\text{Br}_2$. The lowest $\text{Ni}^{\text{II}}((S,S)\text{-}i\text{Pr-pybox})\text{Br}_2$, $\text{Ni}^{\text{II}}((S,S)\text{-}i\text{Pr-pybox})(\text{Me})\text{Br}$, and $\text{Ni}^{\text{II}}((S,S)\text{-}i\text{Pr-pybox})\text{Me}_2$ species are highlighted in red.



Scheme 5.12. Expanded diagram of $\text{Ni}^{\text{III}}((S,S)\text{-}i\text{Pr-pybox})\text{Br}_2((S)\text{-ind})$ methylation as part of the Ni^{III} pathway. All numbers are in kcal/mol and relative to $\text{Ni}^{\text{III}}((S,S)\text{-}i\text{Pr-pybox})\text{Br}_2((S)\text{-ind})$. Red denotes the lowest point and thermodynamic sink, $[\text{Ni}^{\text{III}}((S,S)\text{-}i\text{Pr-pybox})\text{Br}^{\text{eq}}((S)\text{-ind})^{\text{ax}}\text{-Me}^{\text{ax}}\text{-ZnI}(\text{dma})_2]^+$, as well as an alternative thermodynamic sink $\text{Ni}^{\text{III}}((S,S)\text{-}i\text{Pr-pybox})\text{Br}^{\text{ax}}((S)\text{-ind})^{\text{eq}}\text{-Br}^{\text{ax}}\text{-Zn}^{\text{R}}\text{MeI}(\text{dma})$; and green the highest point, $\text{Ni}^{\text{III}}((S,S)\text{-}i\text{Pr-pybox})\text{Br}^{\text{ax}}(\text{ind})^{\text{ax}}\text{Me}^{\text{eq}} + \text{ZnBrI}(\text{dma})$, in the production of $[\text{Ni}^{\text{III}}((S,S)\text{-}i\text{Pr-pybox})(\text{Br})(\text{ind})\text{Me}]$.



Scheme 5.13. The reactions of the various $\text{Ni}^{\text{III}}((S,S)\text{-}i\text{Pr-pybox})(\text{Me})\text{ind}$ species that lead to the reductive elimination of ind-Me . All numbers are in kcal/mol and relative to $[\text{Ni}^{\text{III}}((S,S)\text{-}i\text{Pr-pybox})\text{Br}^{\text{eq}}((S)\text{-ind})^{\text{ax}}\text{-Me}^{\text{ax}}\text{-ZnI}(\text{dma})_2]^+$. The starting point is $\text{Ni}^{\text{III}}((S,S)\text{-}i\text{Pr-pybox})(\text{Br})^{\text{ax}}(\text{ind})^{\text{ax}}\text{Me}^{\text{eq}}$, which was produced at the end of Schemes 5.9 or 5.12; the end point is $\text{Ni}^{\text{I}}((S,S)\text{-}i\text{Pr-pybox})\text{Br}$. Both the starting and end points are highlighted in red. The lowest energy pathways leading to the formation of (*R*)- and (*S*)-1-methylindane are highlighted in green and blue, respectively, when separate and in purple when concurrent.

R	Ni ^{III} ((<i>S,S</i>)-R-pybox)(Me)(ind)Br						[Ni ^{III} (L)(Me--ind)Br] [‡]				Ni ^I (L)Br
	A1		A2		A3		D1		D2		G
	(<i>R</i>)	(<i>S</i>)	(<i>R</i>)	(<i>S</i>)	(<i>R</i>)	(<i>S</i>)	(<i>R</i>)	(<i>S</i>)	(<i>R</i>)	(<i>S</i>)	
Ad	4.9	2.8	2.1	0.0	5.0 ^a	10.3	19.1 ^b	19.6 ^b	21.3	20.0	-23.9
Cy	9.8 ^b	8.1	2.1	0.0	6.7 ^a	11.3	28.5 ^b	28.9 ^b	32.5	32.5	-24.1
Me	5.8	2.1	1.4	0.0	7.7	6.6	20.3	18.9	21.0	19.9	-27.2
Ph	0.0	1.7	1.2	1.2	9.4	8.4	17.7	16.2	19.0	19.0	-21.7
(<i>R</i>)- <i>s</i> Bu	3.8	0.7	2.7	0.0	3.7 ^a	6.8	18.3	15.7	20.5	19.8	-32.1
(<i>S</i>)- <i>s</i> Bu	3.0	1.0	2.3	0.0	8.2	6.1	18.1	17.0	21.3	22.1	-27.5
<i>t</i> Bu	5.0	3.1	2.1	0.0	4.8 ^a	9.8	18.9 ^b	18.9 ^b	21.3	19.9	-25.3
C ₂ H ₄ Ph	2.5	0.9	2.6	0.0	9.5	6.2	17.6	19.4	17.5	20.0	-27.3
pybindox	5.5	2.5	1.3	0.0	5.8	5.0	20.5	18.9	21.0	20.5	-28.0

Table 5.4. Relative energies of the neutral **A**, **D**, and **G** species for various Ni(R-pybox) complexes. All numbers are in kcal/mol. Energies given are relative to the lowest calculated type **A** neutral Ni^{III}(R-pybox)(Me)(ind)Br complex. Numbers in blue are the lowest energy (*R*)-ind geometric isomers for **A** and **D**, whereas numbers in red are the lowest energy (*S*)-ind geometric isomer for **A** and **D**. (L) is ((*S,S*)-R-pybox). a) The Ni-ind bond is very long and likely to be very labile. b) An oxazoline ligand is dissociated from the Ni center in the geometry optimized structure.

R	[Ni ^{III} ((<i>S,S</i>)-R-pybox)(Me)(ind)] ⁺						[Ni ^{III} (L)(Me--ind)] ^{‡†}						[Ni ^I (L)] ⁺
	B1		B2		B3		E1		E2		E3		H
	(<i>R</i>)	(<i>S</i>)	(<i>R</i>)	(<i>S</i>)	(<i>R</i>)	(<i>S</i>)	(<i>R</i>)	(<i>S</i>)	(<i>R</i>)	(<i>S</i>)	(<i>R</i>)	(<i>S</i>)	
Ad	13.6	9.5	6.6	5.3	16.3 ^a	N/A ^{a,c}	21.2	19.1	14.9	16.4	N/A ^c	N/A ^c	-13.0
Cy	8.8	7.5	5.6	5.0	11.7 ^a	10.6 ^a	N/A ^c	N/A ^c	20.3	19.4	26.6	18.8	-15.1
Me	11.1	6.5	3.3	2.9	14.9 ^a	13.2	N/A ^d	N/A ^d	15.2	14.9	17.1	13.8	-5.4
Ph	10.4	6.5	4.3	2.5	15.2 ^a	13.6	14.9	12.6	15.1	14.8	N/A ^c	N/A ^c	-9.7
(<i>R</i>)- <i>s</i> Bu	7.9	5.1	2.7	0.9	16.1 ^a	12.4 ^a	12.5	12.1	13.8	14.0	N/A ^c	N/A ^b	-18.4
(<i>S</i>)- <i>s</i> Bu	9.4	6.7	4.6	3.3	16.0 ^a	13.1	15.4	13.5	15.8	16.0	N/A ^c	N/A ^b	-13.4
<i>t</i> Bu	5.8	10.1	5.9	4.9	N/A ^{a,c}	12.4 ^a	16.1	19.7	16.9	16.7	N/A ^c	20.7	-16.2
C ₂ H ₄ Ph	8.1	0.6	2.6	1.9	15.7 ^a	12.7	14.6	7.0	9.1	9.6	12.1	10.3	-16.3
pybindox	10.8	6.2	2.5	1.5	N/A ^{a,c}	12.6	17.3	16.2	13.7	13.3	N/A ^c	15.2	-11.6

Table 5.5. Relative energies of the cationic **B**, **E**, and **H** species for various Ni(R-pybox) complexes. All numbers are in kcal/mol. Energies given are relative to the lowest calculated type **A** neutral Ni^{III}(R-pybox)(Me)(ind)Br complex. Numbers in blue are the lowest energy (*R*)-ind geometric isomer for **B** and **E**, whereas numbers in red are the lowest energy (*S*)-ind geometric isomer for **B** and **E**. (L) is ((*S,S*)-R-pybox). a) The Ni-ind bond is very long and likely to be very labile. b) Geometry optimized to a Me^{ax}ind^{eq} (**B1/E1**) configuration. c) Geometry optimized to a Me^{eq}ind^{ax} (**B2/E2**) configuration. d) Geometry optimized to a Me^{ax}ind^{ax} (**B3/E3**) configuration.

R	[Ni ^{III} ((<i>S,S</i>)-R-pybox)(Me)(ind)dma) ⁺						[Ni ^{III} (L)(Me--ind)dma) [‡]				[Ni ^I (L)dma) ⁺
	C1		C2		C3		F1		F2		J
	(<i>R</i>)	(<i>S</i>)	(<i>R</i>)	(<i>S</i>)	(<i>R</i>)	(<i>S</i>)	(<i>R</i>)	(<i>S</i>)	(<i>R</i>)	(<i>S</i>)	
Ad	4.1	1.5	0.9	-0.3	4.9 ^a	2.6 ^a	19.3	17.2	N/A ^b	N/A ^b	-25.9
Cy	7.4	6.9	1.3	0.6	4.8 ^a	5.4 ^a	N/A ^b	30.9	N/A ^b	N/A ^b	-27.2
Me	3.8	3.5	3.1	2.5	7.0 ^a	6.4 ^a	N/A ^b	19.2	N/A ^b	N/A ^b	-24.6
Ph	0.4	2.3	2.6	1.7	3.9 ^a	2.8 ^a	17.1	15.8	N/A ^b	N/A ^b	-25.7
(<i>R</i>)- <i>s</i> Bu	1.7	-0.2	3.8	1.6	7.9 ^a	3.2 ^a	N/A ^b	N/A ^b	N/A ^b	N/A ^b	-30.0
(<i>S</i>)- <i>s</i> Bu	1.8	1.9	3.3	1.4	7.1 ^a	4.3 ^a	N/A ^b	16.5	N/A ^b	N/A ^b	-27.3
<i>t</i> Bu	5.8	3.1	2.8	0.8	5.1 ^a	5.6 ^a	19.5	18.3	N/A ^b	N/A ^b	-26.5
C ₂ H ₄ Ph	4.3	2.7	1.2	-0.6	4.5 ^a	4.5 ^a	N/A ^b	14.7	N/A ^b	N/A ^b	-28.2
pybindox	3.7	-0.1	-0.7	-2.6	4.4 ^a	3.5 ^a	17.3	15.0	N/A ^b	N/A ^b	-25.2

Table 5.6. Relative energies of the cationic **C**, **F**, and **J** species for various Ni(R-pybox) complexes. All numbers are in kcal/mol. Energies given are relative to the lowest calculated type **A** neutral Ni^{III}(R-pybox)(Me)(ind)Br complex. Numbers in blue are the lowest energy (*R*)-ind geometric isomer for **C**, whereas numbers in red are the lowest energy (*S*)-ind geometric isomer for **C**. (L) is ((*S,S*)-R-pybox). a) The Ni-ind bond is very long and likely to be very labile. b) A species containing a Ni-dma bond could not be found.

5.8 References

- [1] de Meijere, A.; Diederich, F. *Metal-Catalyzed Cross-Coupling Reactions*, 2nd ed.; Wiley-VCH: Weinheim, Germany; **2004**.
- [2] Tamao, K.; Sumitani, K.; Kumada, M. *J. Am. Chem. Soc.* **1972**, *94*, 4374–4376.
- [3] Heck, R. F.; Nolley, Jr., J. P. *J. Org. Chem.* **1972**, *37*, 2320–2322.
- [4] Sonogashira, K. *J. Organomet. Chem.* **2002**, *653*, 46–49.
- [5] King, A. O.; Okukado, N.; Negishi, E. *J. Chem. Soc. Chem. Comm.* **1977**, *19*, 683–684.
- [6] Stille, J. K. *Angew. Chem. Int. Ed. Engl.* **1986**, *25*, 508–524.
- [7] Miyaura, N.; Yamada, K.; Suzuki, A. *Tet. Lett.* **1979**, *20*, 3437–3440.
- [8] Hatanaka, Y.; Hiyama, T. *J. Org. Chem.* **1988**, *53*, 918–920.
- [9] Fischer, C.; Fu, G. C. *J. Am. Chem. Soc.* **2005**, *127*, 4594–4595.
- [10] Arp, F. O.; Fu, G. C. *J. Am. Chem. Soc.* **2005**, *127*, 10482–10483.
- [11] Smith, S. W.; Fu, G. C. *J. Am. Chem. Soc.* **2008**, *130*, 12645–12647.
- [12] Lin, X.; Sun, J.; Xi, Y.; Lin, D. *Organometallics* **2011**, *30*, 3284–3292.
- [13] (a) Hehre, W. J.; Ditchfield, R.; Pople, J. A. *J. Chem. Phys.* **1972**, *56*, 2257–2261.
(b) Francl, M. M.; Pietro, W. J.; Hehre, W. J.; Binkley, J. S.; Gordon, M. S.; Defrees, D. J.; Pople, J. A. *J. Chem. Phys.* **1982**, *77*, 3654–3665.
- [14] *Angew. Chem. Int. Ed.* **2012**, *51*, 7024–7027.
- [15] Buscagan, T. M.; Schley, N.; Fu, G. C. *Manuscript under preparation*.
- [16] *Jaguar, version 7.9*; Schrödinger, LLC: **2012**, New York, NY.

- [17] (a) Tannor, D. J.; Marten, B.; Murphy, R.; Friesner, R. A.; Sitkoff, D.; Nicholls, A.; Ringnalda, M.; Goddard, W. A.; Honig, B. *J. Am. Chem. Soc.* **1994**, *116*, 11875–11882.
- (b) Marten, B.; Kim, K.; Cortis, C.; Friesner, R. A.; Murphy, R. B.; Ringnalda, M. N.; Sitkoff, D.; Honig, B. *J. Phys. Chem.* **1996**, *100*, 11775–11788.
- [18] Sears, F. W.; Zemansky, M. W.; Young, H. D. *University Physics, 6th Ed.*; Addison-Wesley, **1982**.
- [19] The probe radius r is automatically calculated by *Jaguar* using the formula $r = 0.5833 \sqrt[3]{MW/\rho}$ where MW is the molecular weight and ρ is the density of the solvent.
- [20] (a) Becke, A. D. *Phys. Rev. A.* **1998**, *38*, 3098–3100.
- (b) Becke, A. D. *J. Chem. Phys.* **1993**, *98*, 5648–5652.
- (c) Lee, C. T.; Yang, W. T.; Parr, R. G. *Phys. Rev. B.* **1988**, *37*, 785–789.
- [21] Grimme, S.; Antony, J.; Erlich, S.; Krieg, H. *J. Chem. Phys.* **2010**, *132*, 154104.
- [22] Hay, P. J.; Wadt, W. R. *J. Chem. Phys.* **1985**, *82*, 299–310.
- [23] (a) Hehre, W. J.; Ditchfield, R.; Pople, J. A. *J. Chem. Phys.* **1972**, *56*, 2257–2261.
- (b) Francl, M. M.; Pietro, W. J.; Hehre, W. J.; Binkley, J. S.; Gordon, M. S.; Defrees, D. J.; Pople, J. A. *J. Chem. Phys.* **1982**, *77*, 3654–3665.
- [24] Wertz, D. H. *J. Am. Chem. Soc.* **1980**, *102*, 5316–5322.
- [25] Gopal, R.; Rizvi, S.A. *J. Indian Chem. Soc.* **1968**, *45*, 13–16.
- [26] Ochiai, H.; Jang, M.; Hirano, K.; Yorimitsu, H.; Oshima, K. *Org. Lett.* **2008**, *10*, 2681–2683.